

1 Summertime nitrate aerosol in the upper troposphere and lower stratosphere
2 over the Tibetan Plateau and the South Asian summer monsoon region

3

4

5 Yixuan Gu^{a,b}, Hong Liao^{c,*}, and Jianchun Bian^d

6

7 ^aState Key Laboratory of Atmospheric Boundary Layer Physics and
8 Atmospheric Chemistry (LAPC), Institute of Atmospheric Physics, Chinese
9 Academy of Sciences, Beijing, China.

10 ^bUniversity of Chinese Academy of Sciences, Beijing, China

11 ^cSchool of Environmental Science and Engineering, Nanjing University of
12 Information Science & Technology, Nanjing, China

13 ^dKey Laboratory of Middle Atmosphere and Global Environment Observation
14 (LAGEO), Institute of Atmospheric Physics, Chinese Academy of Sciences,
15 Beijing, China.

16

17

18

19 *Corresponding author address:

20 Prof. Hong Liao

21 School of Environmental Science and Engineering

22 Nanjing University of Information Science & Technology

23 Nanjing 210044, China

24 E-mail: hongliao@nuist.edu.cn

25

26 **Abstract**

27 We use the global three-dimensional Goddard Earth Observing System
28 chemical transport model (GEOS-Chem) to examine the contribution of nitrate
29 aerosol to aerosol concentrations in the upper troposphere and lower
30 stratosphere (UTLS) over the Tibetan Plateau and the South Asian summer
31 monsoon (TP/SASM) region during summertime of year 2005. Simulated
32 surface-layer aerosol concentrations are compared with ground-based
33 observations, and simulated aerosols in the UTLS are evaluated by using the
34 Stratospheric Aerosol and Gas Experiment II satellite data. Simulations show
35 elevated aerosol concentrations of sulfate, nitrate, ammonium, black carbon,
36 organic carbon, and PM_{2.5} (particles with diameter equal or less than 2.5 μm,
37 defined as the sum of sulfate, nitrate, ammonium, black carbon, and organic
38 carbon aerosols in this study) in the UTLS over the TP/SASM region
39 throughout the summer. Nitrate aerosol is simulated to be of secondary
40 importance near the surface but the most dominant aerosol species in the
41 UTLS over the studied region. Averaged over summertime and over the
42 TP/SASM region, C_{NIT} (the ratio of nitrate concentration to PM_{2.5} concentration)
43 values are 5–35% at the surface, 25–50% at 200 hPa, and could exceed 60%
44 at 100 hPa. The mechanisms for the accumulation of nitrate in the UTLS over
45 the TP/SASM region include vertical transport and the gas-to-aerosol
46 conversion of HNO₃ to form nitrate. The high relative humidity and low
47 temperature associated with the deep convection over the TP/SASM region
48 are favorable for the gas-to-aerosol conversion of HNO₃.

49 **1 Introduction**

50 Aerosols in the upper troposphere and lower stratosphere (UTLS) have much
51 longer residence times than those in the lower troposphere, influencing
52 atmospheric chemistry and the Earth's climate with large spatial and temporal
53 coverage (Rasch et al., 2008). Aerosols in the UTLS influence the
54 concentrations of chemical species via changes in photolysis rates and
55 heterogeneous reactions (Pitari et al., 2014). For example, heterogeneous
56 reactions on sulfate aerosol can perturb the chemical partitioning in the lower
57 stratosphere, leading to significant O₃ depletion through enhanced chlorine,
58 bromine, and odd-hydrogen catalytic cycle (Zhao et al., 1997; Considine et al.,
59 2001; Talukdar et al., 2012; Tang et al., 2014; Pitari et al., 2014). Aerosols in
60 the UTLS also influence climate by altering properties of cirrus clouds via
61 homogeneous or heterogeneous ice nucleation (Li et al., 2005; Liu et al., 2009;
62 Yin et al., 2012; Fadnavis et al., 2013). Injection of aerosols into the UTLS has
63 been reported to induce complex responses in circulation, temperature, and
64 water vapor (Liu et al., 2009; Wu et al., 2011; Su et al., 2011; Fadnavis et al.,
65 2013).

66 Aerosols over the Tibetan Plateau (TP) and the Asian summer monsoon
67 region are especially important. The TP is surrounded by countries with large
68 anthropogenic emissions (Li et al., 2005; Lau et al., 2006). Aerosols from India,
69 Southeast Asia, and southern China can be transported to the TP by prevailing
70 winds in the premonsoon and monsoon seasons (Lawrence and Lelieveld,
71 2010; Xia et al., 2011). Observational and modeling studies have shown that
72 persistent maxima of atmospheric constituents, such as water vapor
73 (Gettelman et al., 2004; Randel and Park, 2006; Park et al., 2007), CO (Kar et

74 al., 2004; Li et al., 2005; Park et al., 2007, 2008, 2009), CH₄ (M. Park et al.,
75 2004; Xiong et al., 2009), NO_x (M. Park et al., 2004), HCN (Park et al., 2008;
76 Randel et al., 2010), C₂H₆ and C₂H₂ (Park et al., 2008), exist in the UTLS
77 above the TP and the South Asian summer monsoon (SASM) region because
78 of the deep convection during boreal summer. Satellite observations
79 suggested that the convection associated with the SASM is a vital pathway to
80 transport air mass from the lower troposphere into the stratosphere (Chen et
81 al., 2006; Randel and Park, 2006; Randel et al., 2010; Bian et al., 2011a). The
82 heating associated with the persistent deep convection during summertime
83 leads to the formation of the Tibetan anticyclone in the UTLS, which acts to
84 isolate air within the anticyclone and traps the uplifted pollutants at that altitude
85 (Park et al., 2007; Vernier et al., 2011; Bourgeois et al., 2012; Fadnavis et al.,
86 2013; He et al., 2014). The stratosphere-troposphere exchange (STE) over the
87 TP contributes largely to the global STE (Chen et al., 2006).

88 Previous studies have reported that aerosols exist in the UTLS over the
89 TP/SASM region. Kim et al. (2003) carried out optical measurements with a
90 ground-based lidar in Lhasa from August to October of 1999, and found an
91 enhancement in aerosol concentration near the local tropopause with
92 scattering ratio (SR, the ratio of aerosol plus molecular backscatter to
93 molecular backscatter alone) of 1.1–1.2. Tobo et al. (2007) reported an
94 enhancement of sub-micron aerosols (effective radius $r = 0.15\text{--}0.6\ \mu\text{m}$) near
95 the summertime tropopause (about 130 to 70 hPa), on the basis of in situ
96 balloon measurements from an Optical Particle Counter at the same location in
97 August of 1999. Vernier et al. (2009) examined satellite measurements from
98 the Cloud-Aerosol Lidar with Orthogonal Polarization (CALIOP) onboard

99 Cloud-Aerosol Lidar and Infrared Pathfinder Satellite Observation (CALIPSO)
100 and reported the presence of small depolarizing particles with high SR values
101 (about 1.20 at 532 nm) at 16–17 km altitude over South Asia in July and
102 August of 2007 and 2008. Bourgeois et al. (2012) found that an aerosol layer
103 existed at 16–18 km altitude over the Asian continent and Indian Ocean
104 (20°S–30°N, 5–105°E) on the basis of the CALIOP observations. Recently, He
105 et al. (2014) examined the vertical profiles of aerosol extinction coefficients
106 measured with a Micro Pulse Lidar at Naqu, a meteorological station located in
107 the central part of the TP, and also showed a maximum in aerosol extinction
108 coefficient ($\sim 2.10^{-3} \text{ km}^{-1}$) in the UTLS (18–19 km) during the summer of 2011.

109 A number of previous studies have attempted to understand the chemical
110 composition of aerosols in the UTLS. Froyd et al. (2009) measured aerosol
111 composition with the National Oceanic and Atmospheric Administration (NOAA)
112 single-particle mass spectrometer aboard the National Aeronautics and Space
113 Administration (NASA) WB-57 high altitude aircraft platform, and reported that
114 particles in the tropical tropopause layer were rich in nitrogen. Vernier et al.
115 (2011) suggested that aerosol layer at the tropopause of Asia could be sulfur
116 and/or organics, considering that Asian pollutants consisted of black carbon,
117 organic carbon, SO₂, and NO_x (Park et al., 2009; Randel et al., 2010). Weigel
118 et al. (2011) analyzed the volatility of aerosols obtained from in situ airborne
119 measurements and reported that about 75–90 % of the particles in the tropical
120 tropopause layer were volatile, but this study did not give any detailed
121 analyses of chemical composition of aerosols. Bourgeois et al. (2012) showed,
122 by using the ECHAM5.5-HAM2 model, that sulfate, water, and OC contributed,
123 respectively, 53%, 29%, and 11% to aerosol extinction in the vicinity of the

124 tropical tropopause layer. The ECHAM5.5-HAM2 model used by Bourgeois et
125 al. (2012) simulated all major aerosol species in the atmosphere except for
126 nitrate.

127 Few previous studies have examined nitrate aerosol in the UTLS, although
128 nitrate is expected to be important for the following reasons. First, emissions of
129 precursors of nitrate, such as NO_x and NH_3 , are high over India, Southeast
130 Asia, and China (Streets et al., 2003; Datta et al., 2012; Huang et al., 2012).
131 Second, simulated nitrate concentrations are high over those regions (Liao and
132 Seinfeld, 2005; Mu and Liao, 2014; Lou et al., 2014). Third, measured
133 concentrations of nitrate are comparable to or larger than those of sulfate at
134 rural and urban sites in the SASM region. Shrestha et al. (2000) carried out
135 measurements of aerosols at Phortse, Nepal, during September
136 1996–November 1997, and showed that the average concentration of nitrate
137 during the monsoon season (June–September) was $0.34 \mu\text{g m}^{-3}$, higher than
138 that of sulfate ($0.17 \mu\text{g m}^{-3}$). Decesari et al. (2010) reported, on the basis of
139 measurements at the Nepal Climate Observatory–Pyramid from 2006 to 2008,
140 that the concentrations of nitrate and sulfate were $0.37 \mu\text{g m}^{-3}$ and $0.50 \mu\text{g m}^{-3}$,
141 respectively, during the monsoon season. Chatterjee et al. (2010) measured
142 aerosols at a high altitude station in northeastern Himalayas during
143 January–December 2005. They found that the average concentrations of
144 fine-mode nitrate and sulfate were $3.31 \pm 2.25 \mu\text{g m}^{-3}$ and $3.80 \pm 2.9 \mu\text{g m}^{-3}$,
145 respectively. At Lahore, an urban site in Pakistan, the observed daytime nitrate
146 concentration of $21.8 \mu\text{g m}^{-3}$ was also higher than sulfate concentration of 12.6
147 $\mu\text{g m}^{-3}$ (Lodhi et al., 2009), as the observations were averaged over November
148 2005 to March 2006. Fourth, the low temperatures in the UTLS would favor

149 nitrate formation (Seinfeld and Pandis, 2006). Therefore, it is of interest to take
150 nitrate aerosol into consideration when we examine aerosols in the UTLS.

151 In this work we simulate nitrate aerosol and its contribution to aerosol
152 concentrations in the UTLS over the TP (70–105°E, 25–40°N) and the SASM
153 region (70–105°E, 10–25°N) by using the global chemical transport model
154 GEOS-Chem driven by the assimilated meteorological fields. These regions of
155 interest are shown in Fig. 1. Simulated surface-layer aerosol concentrations
156 are compared with ground-based observations, and simulated aerosols in the
157 UTLS are evaluated by using the Stratospheric Aerosol and Gas Experiment
158 II (SAGE II) satellite data. Section 2 is a brief description of the GEOS-Chem
159 model and numerical experiment. Section 3 presents the simulation and
160 evaluation of distributions and concentrations of HNO₃ and O₃ to show model's
161 capability in simulating the NO_x-O₃-HNO₃ cycle over the studied regions.
162 Section 4 shows simulated aerosols and Section 5 presents the simulated
163 contribution of nitrate to aerosol concentrations in the UTLS over the TP and
164 the SASM region. Section 6 discusses the mechanisms for high concentrations
165 of nitrate in the UTLS. Section 7 discusses the impacts of uncertainties in
166 surface-layer aerosol concentrations on simulated nitrate in the UTLS.

167

168 **2 Model description and numerical experiment**

169 **2.1 GEOS-Chem model**

170 We simulate gas-phase species and aerosols using the global chemical
171 transport model GEOS-Chem (version 9-01-03, <http://geos-chem.org>) driven
172 by the GEOS-5 assimilated meteorological fields from the Goddard Earth
173 Observing System of the NASA Global Modeling and Assimilation Office. The

174 version of the model used here has a horizontal resolution of 2° latitude by 2.5°
175 longitude and 47 vertical layers extending from the surface to 0.01 hPa. Over
176 the TP and the SASM region, the model has about 34 layers in the troposphere
177 and 12 layers in the stratosphere.

178 The GEOS-Chem model has a fully coupled treatment of tropospheric
179 NO_x-CO-hydrocarbon-aerosol chemistry and aerosols including sulfate (SO₄²⁻),
180 nitrate (NO₃⁻), ammonium (NH₄⁺), organic carbon (OC), black carbon (BC) (R. J.
181 Park et al., 2003; 2004; Pye et al., 2009), mineral dust (Fairlie et al., 2007), and
182 sea salt (Alexander et al., 2005; Jaeglé et al., 2011). Anthropogenic aerosols
183 are treated as bulk mass concentrations (particles of SO₄²⁻, NO₃⁻, NH₄⁺, BC,
184 and OC are not size-resolved). Sea Salt mass is simulated for two size bins
185 (0.1–0.5 and 0.5–8 μm) and mineral dust is simulated for four size bins (0.1–
186 1.0, 1.0–1.8, 1.8–3.0, and 3.0–6.0 μm). Both BC and OC consist of hydrophilic
187 and hydrophobic fractions in the model. It is assumed that 80% of BC and 50%
188 of OC emitted from all primary sources are hydrophobic (Cooke et al., 1999;
189 Chin et al., 2002; Chung and Seinfeld, 2002), which become hydrophilic with
190 an e-folding time of 1.2 days following Cooke et al. (1999) and Chin et al.
191 (2002). All secondary OC is assumed to be hydrophilic. Hydrophilic fractions of
192 both BC and OC aerosols are assumed to be fully soluble.

193 The gas-aerosol partitioning of nitric acid and ammonium is calculated
194 using the ISORROPIA II thermodynamic equilibrium module (Fountoukis and
195 Nenes, 2007). In the version of the GEOS-Chem model used in this work, ions
196 considered in ISORROPIA II include H⁺/Na⁺/NH₄⁺/Cl⁻/SO₄²⁻/HSO₄⁻/NO₃⁻/OH⁻. The
197 two-way coupling between aerosols and gas phase chemistry provides
198 consistent chemical fields for aerosol simulation and aerosol mass for

199 heterogeneous processes and calculations of gas-phase photolysis rates.
200 Heterogeneous reactions include hydrolysis of N_2O_5 (Evans and Jacob, 2005),
201 irreversible absorption of NO_3 and NO_2 on wet aerosols (Jacob, 2000), and the
202 uptake of HO_2 by aerosols (Liao and Seinfeld, 2005; Thornton et al., 2008).
203 Aerosol species are treated as an external mixture in the calculation of aerosol
204 optical properties.

205 With respect to chemistry in the stratosphere, stratospheric O_3
206 concentrations are calculated using the linearized parameterization scheme
207 (McLinden et al., 2000). The monthly mean production rates and loss
208 frequencies of other stratospheric species (including long-lived species such
209 as CFCs and N_2O) use those from NASA Global Modeling Initiative (GMI)
210 Combo simulations (Duncan et al., 2007; Considine et al., 2008; Murray et al.,
211 2012).

212 Convective transport in GEOS-Chem mimics that in the parent GEOS
213 general circulation model (GCM) (Hack, 1994; Zhang and McFarlane, 1995),
214 which accounts for updraft, downdraft, and entrainment mass fluxes for deep
215 and shallow convection (Wu et al., 2007). The aerosol wet deposition scheme
216 in the GEOS-Chem follows that of Liu et al. (2001). For the scavenging of
217 aerosols, SO_4^{2-} , NO_3^- , NH_4^+ , and hydrophilic OC and hydrophilic BC aerosols
218 are assumed to be fully soluble. Dry deposition follows the standard
219 resistance-in-series model of Wesely (1989).

220 Global emissions of aerosols and their precursors in the GEOS-Chem
221 follow R. J. Park et al. (2003, 2004), with anthropogenic emissions of NO_x , CO,
222 SO_2 , and non-methane volatile organic compounds (NMVOC) in Asia
223 overwritten by David Streets' 2006 emission inventory

224 (<http://mic.greenresource.cn/intex-b2006>). Emissions of NH₃ in Asia are taken
225 from Streets et al. (2003). Since NH₃ emissions in China showed large
226 uncertainties in previous studies (Streets et al., 2003; Kim et al., 2006; Y.
227 Zhang et al., 2010; Huang et al., 2011, 2012), we use the most recent estimate
228 of NH₃ emissions in China by Huang et al. (2012), which is 9.8 Tg yr⁻¹, instead
229 of 13.5 Tg yr⁻¹ from Streets et al. (2003). Table 1 summarizes the annual
230 emissions of NO_x, SO₂, NH₃, OC, and BC in Asia domain (60–155°E,
231 10–55°N).

232 Natural NO_x emissions from lightning are calculated using the scheme
233 described by Sauvage et al. (2007) and Murray et al. (2012), and those from
234 soil are simulated following Wang et al. (1998). Natural NH₃ emissions from
235 soil, vegetation, and the oceans are taken from the Global Emissions Inventory
236 Activity inventory (Bouwman et al., 1997). Biomass burning emissions are from
237 the monthly Global Fire Emissions Database (GFED v3) driven by satellite
238 observations of fire activity (van der Werf et al., 2010). Biogenic VOC (volatile
239 organic compounds) emissions are calculated from the Model of Emissions of
240 Gases and Aerosols from Nature (Guenther et al., 2006).

241 The monthly variations of emissions of SO₂ and NO_x follow Wang et al.
242 (2013) and those of BC and OC follow Lou et al. (2014). The monthly scaling
243 factors for NH₃ emissions follow the global inventory described in Fisher et al.
244 (2011). Monthly variations of emissions (anthropogenic plus natural emissions)
245 of NO_x SO₂, NH₃, OC, and BC over Asia are displayed in Fig. 2. The emissions
246 of NH₃ are the highest in June as a result of the agriculture practice and high
247 temperatures (Wang et al., 2013).

248 **2.2 Numerical experiment**

249 To examine the contribution of nitrate to aerosol concentrations in the UTLS
250 over the TP/SASM region, we simulate aerosol concentrations by using the
251 emissions of and meteorological fields of year 2005. Year 2005 is chosen so
252 that we can use the observational datasets for this year from SAGE II and MLS,
253 as described in Sects. 3 and 4. Following Rasch et al. (2008), we perform a
254 10-year spin-up run to generate the initial conditions (to allow the stratospheric
255 species to reach quasi-steady state conditions). We would consider that the
256 tropospheric simulation can be representative of year 2005 but stratosphere
257 simulation should represent a multi-year average, because the production
258 rates and loss frequencies in the stratosphere are the averages over years of
259 2004–2010 ([http://wiki.seas.harvard.edu/geos-chem/index.php/Stratospheric_](http://wiki.seas.harvard.edu/geos-chem/index.php/Stratospheric_chemistry)
260 [chemistry](http://wiki.seas.harvard.edu/geos-chem/index.php/Stratospheric_chemistry)).

261

262 **3 Simulated concentrations of HNO₃ and O₃ and model evaluation**

263 Nitrate aerosol forms when nitric acid (HNO₃) reacts with alkaline gases (for
264 example, ammonia) in the atmosphere (Seinfeld and Pandis, 2006). HNO₃, as
265 the important precursor of nitrate, is the major oxidation product of nitrogen
266 oxides (NO_x = NO+NO₂) (Seinfeld and Pandis, 2006). To show the model's
267 capability in simulating the NO_x-O₃-HNO₃ cycle over the studied regions, we
268 present and evaluate the simulated HNO₃ and O₃ in this section.

269 Simulated mixing ratios of HNO₃ and O₃ in the UTLS are evaluated by
270 using datasets from the limb viewing satellite instrument of Microwave Limb
271 Sounder (MLS, version 3.3, level 2,
272 ftp://acdisc.gsfc.nasa.gov/data/s4pa///Aura_MLS_Level2/). The MLS datasets
273 provide valuable information on atmospheric compositions in the UTLS

274 (Waters et al., 2006). For HNO₃, the MLS provides scientifically useful datasets
275 for 215 to 1.5 hPa, with a vertical resolution of 3–4 km and a horizontal
276 resolution of 400–500 km. Since further evaluations are needed for datasets at
277 altitudes with pressures higher than 215 hPa (Livesey et al., 2011), we use
278 only datasets for pressures lower than that. For O₃, the MLS provides
279 scientifically useful datasets for 261 to 0.02 hPa, with a vertical resolution of
280 2.5–3 km and a horizontal resolution of 300–400 km in the UTLS (Santee et al.,
281 2007; Livesey et al., 2011). The uncertainties of the MLS HNO₃ and O₃
282 datasets in the UTLS are discussed in Livesey et al. (2011). The MLS data
283 HNO₃ product at 100 hPa represents an average of a 3–4 km layer reaching
284 from below the tropopause layer into the lower stratosphere (Duncan et al.,
285 2007). The data screening is conducted strictly according to the instructions of
286 Livesey et al. (2011). For comparison with the MLS observations, the
287 simulated HNO₃ and O₃ mixing ratios are converted to \hat{x} , following the method
288 of Livesey et al. (2011):

$$\hat{x} = x_a + A(x - x_a)$$

289 where A is the averaging kernel matrix of the MLS, x is the modeled vertical
290 profile of HNO₃ or O₃ interpolated at the vertical grid of MLS, and x_a is the
291 HNO₃ or O₃ prior profile of MLS.

292 **3.1 HNO₃**

293 Figure 3(a) shows the simulated global distribution of HNO₃ concentrations
294 averaged over June-August of 2005. Concentrations of HNO₃ exceed 1 ppbv
295 over the industrialized areas such as Europe, North America, central and
296 eastern Asia, and over biomass burning regions in the tropics, in agreement
297 with the distributions and magnitudes reported in Liao et al. (2003). Over South

298 Asia, simulated HNO₃ concentrations are high (0.3–1 ppbv) in the northern
299 Indian subcontinent, because the emissions of NO_x and NH₃ are high in this
300 region (Streets et al., 2003; Zhang et al., 2009; Datta et al., 2012).

301 Figures 4(a)-4(b) show the simulated HNO₃ concentrations in the UTLS
302 averaged over June-August of 2005. Since the tropopause is located at
303 70–150 hPa (12–15 km) over the TP/SASM region (Li et al., 2005; Bian et al.,
304 2011b; Fadnavis et al., 2014), we choose the vertical layers of 200 hPa and
305 100 hPa to represent the UTLS. At both 200 hPa and 100 hPa, the highest
306 HNO₃ concentrations are simulated to occur in the high latitude regions in the
307 Northern Hemisphere (NH) (Fig. 4(a) and Fig. 4(b)). Simulated HNO₃
308 concentrations at 100 hPa are low over the region of 40–100°E and 10–30°N,
309 which is part of the anticyclone region defined in Fig. 1. Figure 4(c) shows the
310 latitude-altitude cross section of simulated seasonal mean HNO₃ mixing ratios
311 averaged over 70–105°E. In boreal summer, the highest HNO₃ mixing ratios
312 are simulated to occur at 30 hPa over the Polar Regions in both hemispheres.
313 Over high latitudes, HNO₃ concentrations in the Southern Hemisphere (SH)
314 are simulated to be higher than those in the NH.

315 To evaluate the simulated HNO₃, Figures 4(d)-4(f) show HNO₃
316 concentrations in the UTLS from MLS that are averaged over June-August of
317 2005. At 200 and 100 hPa altitudes, the observed HNO₃ mixing ratios are high
318 in the high latitudes in the NH, which are captured by the GEOS-Chem model.
319 The observed HNO₃ at 100 hPa exhibits low values of less than 400 pptv over
320 30–100°E and 10–30°N in the Asian monsoon anticyclone region (Fig. 4(e)). At
321 100 hPa, the observed HNO₃ mixing ratio averaged over the TP/SASM region
322 (70–105°E, 10–40°N) is 335.4 pptv, which is lower than the simulated value of

323 372.6 pptv. Considering all the grid cells with MLS HNO₃ data available, the
324 simulated seasonal mean HNO₃ concentrations show normalized mean bias
325 (NMB) of +11.1 % at 100 hPa over the TP/SASM region in summer of year
326 2005. The observed pattern of the HNO₃ vertical distribution (Fig. 4(f)) is also
327 captured by the GEOS-Chem model (Fig. 4(c)). The distributions of HNO₃ in
328 the UTLS are associated with the Brewer-Dobson circulation proposed by
329 Brewer (1949) and Dobson (1956), traveling upwards across the tropopause to
330 the stratosphere at the equator and downwards to the troposphere near the
331 Polar region.

332 **3.2 O₃**

333 Figure 3(b) shows the global distribution of simulated summertime
334 surface-layer O₃ concentrations. Simulated O₃ concentrations are in a range of
335 40–70 ppbv over Europe, North America, China, and the biomass burning
336 region of South Africa. Our model results agree closely with the simulated
337 distributions and magnitudes reported in Mickley et al. (1999), Collins et al.,
338 (2000), Liao et al. (2003), Wu et al., (2008), Zeng et al. (2008), and Fadnavis et
339 al. (2014). Fadnavis et al. (2014) also presented aircraft measurements over
340 India in September of 2010 during the Cloud Aerosol Interaction and
341 Precipitation Enhancement Experiment (CAIPEEX). Our simulated O₃
342 concentrations of 30–40 ppbv over India agree with the CAIPEEX
343 measurements.

344 Figures 5(a)-5(b) show the simulated O₃ concentrations in the UTLS
345 averaged over June-August of 2005. The distributions of O₃ concentrations in
346 the UTLS are similar to those of HNO₃, with elevated values in the high
347 latitudes of the NH. Relatively low O₃ mixing ratios of less than 200 ppbv are

348 simulated at 100 hPa over 10–30°N, 20–110°E, within the anticyclone region
349 defined in Fig. 1. Our simulated distributions and magnitudes of O₃ agree with
350 those reported in Bian et al. (2011b), which examined the summertime
351 distributions of O₃ in the UTLS during 2005–2009 by using the MLS version 2.2
352 level 2 products (Livesey et al., 2008). Because the background O₃
353 concentrations are generally high in the UTLS and the stratosphere, the low O₃
354 concentrations in the UTLS over the TP/SASM region are caused by the deep
355 convection that transports O₃-poor air upward (Fu et al., 2006; Randel and
356 Park, 2006; Park et al., 2007; Bian et al., 2011b). Figure 5(c) displays the
357 latitude-altitude cross section of seasonal mean O₃ mixing ratios averaged
358 over 70–105°E. As a result of the Brewer-Dobson circulation, O₃
359 concentrations in the UTLS are lower over the tropics than in the Polar
360 Regions, even though the maximum O₃ concentrations are located around 10
361 hPa over the tropics (Brewer, 1949). Our simulated O₃ concentrations in the
362 UTLS agree well with the measurements from MLS (Fig. 5(d)-5(f)). At 100 hPa,
363 simulated and MLS observed O₃ mixing ratios averaged over the TP/SASM
364 region (70–105°E, 10–40°N) are 151.7 and 146.6 ppbv, respectively.
365 Compared to MLS observations, simulated O₃ concentrations at 100 hPa have
366 a NMB of +3.5 % over the TP/SASM region in summer of 2005. Our simulated
367 global STE of O₃ is 420 Tg yr⁻¹, which is within the range reported in previous
368 studies (475±120 Tg yr⁻¹ in McLinden et al. (2000), 420 Tg yr⁻¹ in Škerlak et al.
369 (2014), and 556±154 Tg yr⁻¹ in Stevenson et al. (2006)).

370 In addition to the comparisons against MLS products, the simulated O₃
371 profiles are compared with balloon-borne sonde measurements in Fig. 6. The
372 measurements were carried out at Kunming (KM, 102.7°E, 25.0°N) in August

373 of 2009 and 2012, and at Lhasa (LH, 91.1°E, 29.7°N) in August of 2010 and
374 2013. The uncertainties of the observed O₃ mixing ratios were estimated to be
375 within 5–10% (Bian et al. 2012). The comparisons with multi-year observations
376 show that the model can reproduce the vertical distributions of O₃ above 12 km
377 in Kunming and Lhasa. At 100 hPa, the simulated monthly mean O₃ mixing
378 ratio in KM is 112.6 ppbv, and the observed value is 124.2 ppbv in 2009 and
379 113.5 ppbv in 2012. In LH, the simulated monthly O₃ mixing ratio at 100 hPa is
380 152.6 ppbv, and the observed O₃ mixing ratio at that altitude is 142.4 ppbv in
381 2010 and 167.9 ppbv in 2013. The magnitudes of O₃ mixing ratios from these
382 balloon-borne sonde measurements support those from MLS; O₃ mixing ratios
383 in the UTLS are less than 200 ppbv over the TP/SASM region.

384

385 **4 Simulated aerosols and model evaluation**

386 **4.1 Simulated aerosols**

387 Figure 7 (a) shows the simulated surface-layer concentrations of SO₄²⁻, NO₃⁻,
388 NH₄⁺, OC, BC, and PM_{2.5} (the sum of the mass of SO₄²⁻, NO₃⁻, NH₄⁺, BC, and
389 OC aerosols) averaged over June-August of year 2005. As expected,
390 simulated aerosol concentrations are high over polluted regions such as India
391 and eastern China as a result of the high anthropogenic emissions of aerosol
392 precursors and aerosols (Streets et al., 2003; Huang et al., 2012). Over the
393 TP/SASM region (70–105°E, 10–40°N), the average concentrations of SO₄²⁻,
394 NO₃⁻, NH₄⁺, BC, and OC are 1.70, 0.94, 0.85, 0.30, and 0.94 μg m⁻³,
395 respectively. NO₃⁻ is simulated to be of secondary importance at the surface
396 over the region of our interest. The simulated distributions and magnitudes of
397 these aerosol species are similar to those reported in Wang et al. (2013) and

398 Mu and Liao (2014).

399 Figures 7(b) and 7(c) also show the simulated concentrations of SO_4^{2-} ,
400 NO_3^- , NH_4^+ , OC, BC, and $\text{PM}_{2.5}$ in the UTLS. Elevated concentrations of SO_4^{2-} ,
401 NO_3^- , NH_4^+ , OC, BC and $\text{PM}_{2.5}$ are simulated over the TP and Plateau south
402 slope at 200 hPa altitude, and extend from eastern Mediterranean to western
403 China at 100 hPa. The simulated enhanced concentrations of SO_4^{2-} , OC, and
404 BC at 100 hPa over the anticyclone region (20–120°E, 10–40°N) agree with
405 previous observational and modeling studies (Lelieveld et al., 2001; Li et al.,
406 2005; Fadnavis et al., 2013). Li et al. (2005) reported elevated CO
407 concentrations in the upper troposphere over the TP, on the basis of both MLS
408 measurements and the GEOS-Chem simulation for September 2004.
409 Fadnavis et al. (2013) also simulated maximum concentrations of SO_4^{2-} , OC,
410 BC, and mineral dust aerosols in the UTLS during the Asian summer monsoon
411 season owing to convective uplifting of the boundary layer pollutants. With
412 NO_3^- aerosol accounted for in our simulation, NO_3^- is simulated to be the most
413 dominant aerosol species in the UTLS over the TP/SASM region, followed
414 by SO_4^{2-} , NH_4^+ , OC, and BC. At 100 hPa, the averaged concentrations of SO_4^{2-} ,
415 NO_3^- , NH_4^+ , OC, and BC over the TP/SASM region (70–105°E, 10–40°N)
416 region are 0.026, 0.069, 0.014, 0.011, and 0.002 $\mu\text{g m}^{-3}$, respectively.

417 **4.2 Comparisons of simulated aerosol concentrations with in-situ** 418 **observations**

419 The simulated aerosol concentrations in East Asia in the GEOS-Chem model
420 have been evaluated in previous studies (L. Zhang et al., 2010; Fu et al., 2012;
421 Jeong and Park, 2013; Jiang et al., 2013; Wang et al., 2013; Lou et al., 2014).
422 Here we are focused on the evaluation of aerosols in the South Asian

423 monsoon region. For lack of publicly accessible in situ measurements of
424 summertime aerosols in South Asia monsoon area, we compiled monthly or
425 seasonal mean measured concentrations of each aerosol species based on
426 measurements reported in the literature (see Table S1 in the Supplementary
427 Material). These measurements were carried out over years of 1992–2010.
428 The locations of sites with measurements available are shown in Fig. 8(a).
429 Most sites are located in the upwind directions of the TP, with pollutants that
430 can be transported to the UTLS during the South Asian summer monsoon
431 season. The observed PM_{10} concentrations listed in Table S1 are multiplied by
432 0.6 to convert to $PM_{2.5}$ for model evaluation, following the suggestions in
433 Zhang et al. (2002) and Chatterjee et al. (2010).

434 Figures 8(b)–8(f) show the scatterplots of simulated versus observed
435 seasonal mean aerosol concentrations. Compared with measurements,
436 simulated SO_4^{2-} , NO_3^- , NH_4^+ , OC and BC have NMBs of -17.0% , $+38.8\%$,
437 $+42.0\%$, -69.7% and -41.0% , respectively, as the concentrations of all
438 seasons are considered. The correlations between model results and
439 observations have R values of 0.49–0.85 for all aerosol species, indicating that
440 the model is capable of capturing the spatial distributions and seasonal
441 variations of each aerosol species in the South Asian monsoon region despite
442 the biases in concentrations. If we consider simulated and measured
443 concentrations for JJA alone, the simulated concentrations of SO_4^{2-} , NO_3^- ,
444 NH_4^+ , OC and BC exhibit seasonal NMBs of -14.7% , $+51.5\%$, $+74.9\%$, -57.2%
445 and -32.2% , respectively, and the values of R are in the range of 0.24–0.85.
446 Note that the measurements of NO_3^- and NH_4^+ are quite limited in terms of the
447 number of samples, and the discrepancies between model results and

448 measurements may also arise from the mismatch of the model year 2005 with
449 the years of 1992–2010 with observations available.

450 **4.3 Comparisons of simulated aerosol extinction coefficients with SAGE**

451 **II datasets**

452 Satellite datasets from the Stratospheric Aerosol and Gas Experiment II
453 (SAGE II, https://eosweb.larc.nasa.gov/project/sage2/sage2_v620_table) are
454 used to evaluate the simulated aerosol extinction in the UTLS. The SAGE II
455 instrument was launched in October 1984 aboard the Earth Radiation Budget
456 Satellite (ERBS) and terminated on 8 September 2005 (McCormick et al. 1987;
457 Chu et al. 1989). The datasets used here are aerosol extinction coefficients at
458 525 nm from the version 6.20 SAGE retrievals, covering from 0.5 to 40 km with
459 a vertical resolution of 0.5 km. Many validation studies have been conducted
460 on the SAGE II aerosol data (Russell and McCormick, 1989; Oberbeck et al.,
461 1989; Wang et al., 1989), which indicated that extinction coefficients have
462 uncertainties of 20–30%. The extinction coefficients of aerosols in the
463 GEOS-Chem model are calculated using aerosol mass concentration,
464 extinction efficiency, effective radius, particle mass density, and the assumed
465 aerosol size distribution (Drury et al., 2010). The hygroscopic growth of each
466 aerosol species with relative humidity is accounted for, using the hygroscopic
467 growth factors listed in Martin et al. (2003).

468 Figure 9(a) presents the simulated monthly mean distribution of aerosol
469 extinction coefficients at 100 hPa for July of 2005. At 100 hPa, the simulated
470 aerosol extinction coefficients are relatively high over the anticyclone region,
471 where anthropogenic aerosol species (Fig. 7) and natural aerosols such as
472 mineral dust and sea salt contribute to aerosol extinction coefficients in

473 summer. Note that the contributions of sulfate, nitrate, ammonium, OC, sea
474 salt, and mineral dust are all considered when we calculate aerosol extinction
475 coefficients. Aerosol extinction coefficients are simulated to be $1.2\text{--}2\times 10^{-3}$
476 km^{-1} at 100 hPa over the Asian continent and Indian Ocean ($20^{\circ}\text{S}\text{--}30^{\circ}\text{N}$,
477 $30^{\circ}\text{--}105^{\circ}\text{E}$). These values agree closely with aerosol extinction coefficients
478 measured at Naqu during August of 2011 for the same altitude, the maximum
479 of which was $2.4\times 10^{-3} \text{ km}^{-1}$ (He et al., 2014). Vernier et al. (2011) also
480 identified this Asian aerosol layer with high SR at 100 hPa by observations of
481 CALIPSO for JJA of 2006–2008.

482 Figure 9(b) displays the monthly mean vertical profiles of aerosol extinction
483 coefficients averaged over the Asian monsoon anticyclone region ($20\text{--}120^{\circ}\text{E}$
484 $10\text{--}40^{\circ}\text{N}$) (Fig. 1) for July of 2005. The SAGE II datasets are available for July
485 only in 2005. The profiles from SAGE II and the GEOS-Chem simulation are all
486 shown. The vertical distributions of aerosol extinction coefficients “with nitrate”
487 and “without nitrate” are both from the baseline run with full chemistry. The
488 vertical distribution of aerosol extinction coefficient “with nitrate” (or “without
489 nitrate”) indicates that the contribution of nitrate aerosol to aerosol extinction is
490 (or is not) accounted for. Accounting for all aerosol species, the GEOS-Chem
491 model reproduces well the aerosol extinction coefficients above 10 km, but the
492 discrepancies are rather large in altitudes less than 10 km. Note that the
493 uncertainties in satellite datasets increase as the altitude decreases
494 (Vanhellemont et al., 2008; Kulkarni and Ramachandran, 2015), and the
495 missing data in the lower troposphere along the satellite trajectories over the
496 region of our interest also contribute to the discrepancies

497 Comparisons of profiles of aerosol extinction coefficients with and without

498 nitrate aerosol indicate that the profiles show small differences in altitudes less
499 than 6 km but large discrepancies from 6 km to the tropopause. With nitrate
500 aerosol accounted for, the simulated aerosol extinction coefficients agree
501 closely with SAGE II datasets in the UTLS (averaged over 14–16 km, the
502 simulated value is $8.6 \times 10^{-4} \text{ km}^{-1}$ while the observed value is $8.0 \times 10^{-4} \text{ km}^{-1}$).
503 Without nitrate aerosol, the simulated aerosol extinction coefficient at 14–16
504 km altitude is $1.5 \times 10^{-4} \text{ km}^{-1}$, which underestimates the aerosol extinction
505 coefficient by 82.6% compared to that calculated with all the aerosol species.
506 These comparisons of extinction coefficients with and without nitrate aerosol
507 suggest that nitrate aerosol plays an important role in aerosol extinction in the
508 UTLS over the region of our interest.

509

510 **5 Contribution of nitrate to aerosol concentrations in the UTLS**

511 Since nitrate aerosol is simulated to be the most abundant aerosol species in
512 the UTLS over the TP/SASM region, we analyze the contribution of nitrate to
513 $\text{PM}_{2.5}$ concentration ($C_{\text{NIT}} = \text{nitrate concentration} / \text{PM}_{2.5} \text{ concentration}$) in this
514 section. Figure 10 shows the simulated seasonal mean distributions of C_{NIT} for
515 June-August of year 2005. At the surface layer (Fig. 10(a)), simulated high C_{NIT}
516 values are located over the areas with high nitrate concentrations (India and
517 eastern China) as well as the oceans where NO_3^- also forms on sea salt and
518 mineral dust particles (Arimoto et al., 1996; Nakamura et al., 2005; George and
519 Nair, 2008). Over the TP/SASM region, the C_{NIT} values in JJA are 5–35% at the
520 surface, 25–50% at 200 hPa (Fig. 10(b)), and could exceed 60% at 100 hPa
521 (Fig. 10(c)). The latitude-altitude cross section of C_{NIT} (Fig. 10(d)) shows that
522 C_{NIT} over 20–40°N increases with altitude and reaches maximum values

523 around the extratropical tropopause.

524 Table 2 lists the mean concentrations of SO_4^{2-} , NO_3^- , NH_4^+ , BC and OC, and
525 their contributions to $\text{PM}_{2.5}$ during summertime of 2005 over the TP/SASM, TP,
526 and SASM regions. Over the TP/SASM region, SO_4^{2-} , NO_3^- , NH_4^+ , BC and OC
527 are simulated to contribute 35.9%, 19.8%, 18.1%, 6.4%, and 19.8%,
528 respectively, to $\text{PM}_{2.5}$ mass concentration at the surface layer. The
529 contributions increase significantly in the UTLS. The largest C_{NIT} is simulated
530 in the SASM region at 100 hPa, where NO_3^- accounts for 60.5% of $\text{PM}_{2.5}$ mass
531 concentration. The high C_{NIT} values indicate that NO_3^- plays an important role
532 in the aerosol layer in the UTLS over the TP/SASM region.

533 Considering the large uncertainties in simulated sea salt (Jaeglé et al.,
534 2011) and mineral dust (Fairlie et al., 2007) aerosols, we tend to be focused on
535 anthropogenic aerosol species (SO_4^{2-} , NO_3^- , NH_4^+ , BC, and OC) in this work. In
536 our model, concentrations of sea salt (or mineral dust) are simulated to be
537 $1.0\text{--}1.7 \text{ ng m}^{-3}$ (or $5.0\text{--}7.0 \text{ ng m}^{-3}$) over the studied region in the summer of
538 2005, which contribute less than 1.2% (or 5.0%) to total aerosol mass at 100
539 hPa. Therefore the consideration of sea salt and mineral dust can slightly
540 reduce C_{NIT} values, but C_{NIT} values at 100 hPa are still as high as 45-65% over
541 the TP/SASM region in summer.

542

543 **6 Mechanisms for high nitrate concentrations in the UTLS**

544 **6.1 Upward transport of nitrate from the lower troposphere**

545 The intense convective transport of chemical species into the UTLS over the
546 TP/SASM region during summertime has been widely discussed in previous
547 studies (Randel et al., 2010; Bian et al., 2011a; Fadnavis et al., 2013, 2014;

548 Qie et al., 2014; He et al., 2014), evidenced by both the satellite observations
549 (Fu et al., 2006; Luo et al., 2011) and the calculation of the outgoing long-wave
550 radiation which is a convective proxy over the region (Randel and Park, 2006;
551 Park, et al., 2007; Fadnavis et al., 2013). Since nitrate aerosol is simulated to
552 be of secondary abundant aerosol species in the surface layer over the
553 TP/SASM region (Fig. 7), the vertical mass transport through the deep
554 convection in this region contributes to the accumulation of NO_3^- in the UTLS.
555 Figure 11 shows the latitude-altitude cross sections of simulated
556 concentrations of SO_4^{2-} and NO_3^- averaged over 70–105°E in June-August of
557 2005, together with the wind vectors obtained from the European Centre for
558 Medium-Range Weather Forecasts (ECMWF) ERA-Interim Reanalysis data.
559 Note that the assimilated GEOS-5 meteorological fields do not have vertical
560 winds
561 (http://wiki.seas.harvard.edu/geos-chem/index.php/List_of_GEOS-5_met_fields
562 s), so we use the ECMWF reanalysis wind fields to do the analysis here. High
563 values of aerosol concentrations are found on the south slope of the
564 Himalayas, where the deep convection exists. Although both SO_4^{2-} and NO_3^-
565 are transported upward to the extratropical tropopause, the details of the
566 vertical distributions are different. At altitudes higher than 8 km, the
567 concentrations of NO_3^- do not decrease with altitude as quickly as those of
568 SO_4^{2-} , and the concentrations of NO_3^- over 10–40°N are higher than those of
569 SO_4^{2-} .

570 The chemical mechanisms for the formation of SO_4^{2-} , NO_3^- , and NH_4^+
571 aerosols in the GEOS-Chem model were described in R. J. Park et al. (2004),
572 which are comprehensive and have been used extensively in previous studies

573 to simulate these three aerosol species (R. J. Park et al., 2004; Pye et al.,
574 2009; L. Zhang et al., 2010; Zhu et al., 2012; Jiang et al., 2013; Lou et al.,
575 2014). Sulfate aerosol forms from gas-phase oxidation of SO₂ by OH and from
576 in-cloud oxidation of SO₂ by O₃ and H₂O₂. Nitrate forms from the partitioning of
577 HNO₃ between gas and aerosol phases, which is calculated by the
578 ISORROPIA II thermodynamic equilibrium module (Fountoukis and Nenes,
579 2007) in the GEOS-Chem model. HNO₃ is produced by the reaction of NO₂
580 with OH during daytime and by hydrolysis of N₂O₅ on aerosol surfaces at night
581 (Table 3). The chemical mechanisms for SO₄²⁻ and NO₃⁻ have different
582 sensitivity to meteorological conditions. During the vertical transport,
583 temperature decreases, which reduces the gas-phase oxidation of SO₂ (Yao et
584 al., 2002; Seinfeld and Pandis 2006) but promotes the formation of NO₃⁻ by
585 shifting gas-particle equilibria (Dawson et al., 2007; Liao et al., 2009). Dawson
586 et al. (2007) examined the sensitivities of sulfate and nitrate concentrations to
587 temperature by using the Particulate Matter Comprehensive Air Quality Model
588 with extensions (PMCAMx). The sensitivity test was performed by fixing all
589 meteorological parameters but perturbing temperature. Their sensitivity
590 simulations showed that the increases in temperature led to increases in
591 sulfate concentrations and decreases in nitrate concentrations. Compared to
592 nitrate, sulfate concentrations showed smaller sensitivity to temperature
593 changes (Dawson et al., 2007); as temperature increased, nitrate
594 concentrations decreased by 19% K⁻¹ and 17% K⁻¹ in January and July
595 respectively, while sulfate concentration increased by 0.12% K⁻¹ and 1.3% K⁻¹
596 in January and July, respectively. Therefore the different chemical mechanisms
597 for SO₄²⁻ and NO₃⁻ formation contribute to the differences in their vertical

598 distributions.

599 **6.2 Net chemical production of HNO₃ during the vertical transport**

600 As mentioned above, the formation of gas-phase HNO₃ and the partitioning of
601 HNO₃ between gas and aerosol phases are the two major chemical processes
602 that influence NO₃⁻ concentrations. The ability of the GEOS-Chem model to
603 simulate gas-phase HNO₃ has been evaluated in Section 3.1 (by comparisons
604 of our model results with MLS observations and concentrations from previous
605 modeling studies). Major reactions for the production and loss of HNO₃ are
606 listed in Table 3. Figure 12 shows the net chemical production of HNO₃ by
607 gas-phase reactions and heterogeneous reactions (chemical production by
608 reactions R1-R23 minus chemical loss by reactions R24-R25 in Table 3)
609 summed over the TP/SASM region. The net chemical production has an
610 overall trend of decreasing with altitude.

611 **6.3 The gas-to-aerosol conversion of HNO₃ to form nitrate during the** 612 **vertical transport**

613 NO₃⁻ formation from gas-to-aerosol conversion of HNO₃ is calculated by using
614 the ISORROPIA II thermodynamic equilibrium module (Fountoukis and Nenes,
615 2007). As shown in Fig. 12, nitrate formation from gas to aerosol conversion of
616 HNO₃ peaks between 100–300 hPa. The magnitude of gas to aerosol
617 conversion of HNO₃ is several times higher than the net chemical production of
618 HNO₃, indicating that the gas-aerosol partitioning plays a dominant role in the
619 enhancement of nitrate in the UTLS.

620 The gas-to-aerosol conversion of HNO₃ to form NO₃⁻ is very sensitive to
621 relative humidity (RH) and temperature (Fountoukis and Nenes 2007; Dawson
622 et al., 2007). Low temperature and high RH are favorable for NO₃⁻ formation.

623 Figure 13 shows the seasonal mean horizontal distributions of RH and
624 temperature at 100 hPa and the latitude-altitude cross sections of these two
625 parameters averaged over 70–105°E. RH exhibits high values in the TP/SASM
626 region, which are consistent with the high H₂O mixing ratios in this area
627 reported in Gettelman et al. (2004), M. Park et al. (2004), and Fu et al. (2006).
628 At 100 hPa, the locations with high RH of exceeding 45% correspond well with
629 those with high C_{NIT} values (Fig. 10(c)). The latitude-altitude cross section of
630 RH (Fig. 13(c)) shows that RH has high values over the places with intense
631 upward transport (Fig. 11). For temperature, as Fig. 13(b) and 13(d) show,
632 summertime temperatures are cold (190–200 K) at 100 hPa in the TP/SASM
633 region, consistent with the distribution and magnitude reported for August,
634 2011, in He et al. (2014) on the basis of the NCEP Reanalysis data. The low
635 temperatures over the TP/SASM region are associated with the adiabatic
636 expansion of ascending air mass of the deep convections (Yanai et al., 1992;
637 Park et al., 2007; He et al., 2014).

638 Because of the favorable conditions of RH and temperature, the
639 gas-to-aerosol conversion of HNO₃ to form nitrate can occur during the upward
640 transport and in the UTLS. Figure 14 shows the mass budget for nitrate
641 aerosol within the selected box of (70–105°E, 10–40°N, 8–16 km) to see the
642 role of nitrate formation over the TP/SASM region. The horizontal mass fluxes
643 have a net negative value of 0.10 Tg season⁻¹, reducing nitrate aerosol in the
644 selected box. The vertical transport and the gas-to-aerosol conversion of
645 HNO₃ increase nitrate mass in the selected box, with values of 0.09 Tg
646 season⁻¹ and 0.11 Tg season⁻¹, respectively, indicating that the gas-to-aerosol
647 conversion plays an important role in the enhancement of nitrate in the UTLS

648 over the TP/SASM region. Although relatively high RH exists near the
649 tropopause of the TP/SASM region, the air near the tropopause is still dryer
650 compared to that in the lower altitudes. Model results show that the
651 gas-to-aerosol partition of HNO_3 decreases with altitude over 8–16 km,
652 indicating that the gas to aerosol conversion contributes to nitrate
653 accumulation in the UTLS mainly during the process of upward transport.

654 Previous studies have also reported that nitric acid trihydrates (NAT,
655 $\text{HNO}_3 \cdot (\text{H}_2\text{O})_3$) could form in the polar and tropical stratosphere at low
656 temperatures through two mechanisms: (1) the homogeneous nucleation out
657 of supercooled ternary solutions, and (2) the heterogeneous formation on ice
658 particles (Hofmann et al., 1989; Carslaw et al., 1998; Voigt et al., 2000; Popp et
659 al., 2006; Kirner et al., 2011). A typical NAT condensation temperature is
660 approximate 193 K (Kirner et al., 2011). As shown in Fig. 13, the temperatures
661 around 100 hPa over the TP/SASM region are in the range of 190–200 K,
662 which are low enough to produce some NAT particles. However, balloon-borne
663 measurements of depolarization ratio and backscattering ratio of aerosols at
664 Lhasa during August-October of 1999 by Kim et al. (2003) and Tobo et al.
665 (2007) suggested that coarse and aspherical particles such as NAT are scarce
666 in the UTLS of the TP/SASM.

667

668 **7 Sensitivities of simulated nitrate in the UTLS to anthropogenic NO_x ,** 669 **NH_3 , and SO_2 emissions in Asia**

670 Since simulated SO_4^{2-} , NO_3^- and NH_4^+ concentrations have, respectively,
671 NMBs of -17.0% , $+38.8\%$, and $+42.0\%$ on an annual mean basis and of
672 -14.7% , $+51.5\%$, and $+74.9\%$ in summer (Section 4.2), we perform four

673 sensitivity simulations to examine the impacts of uncertainties in surface-layer
674 aerosol concentrations on simulated nitrate in the UTLS. In the first three
675 cases, anthropogenic emissions of NO_x , NH_3 , and SO_2 in Asia are changed by
676 -50% , -50% , and $+20\%$, respectively, relative to those in our standard
677 simulation. In the last case, anthropogenic emissions of all these three species
678 are changed simultaneously, with NO_x reduced by 50%, NH_3 reduced by 50%,
679 and SO_2 increased by 20% in Asia relative to the standard case. The purpose
680 of these sensitivity studies is to reduce NMBs of simulated surface-layer
681 concentrations of SO_4^{2-} , NO_3^- and NH_4^+ and see whether NO_3^- is still the
682 most dominant aerosol species in the UTLS. Model results from these
683 sensitivity studies for summer of 2005 are presented in Table 4.

684 As anthropogenic emissions of SO_2 in Asia are increased by 20%, the
685 NMB of simulated surface-layer SO_4^{2-} concentrations is -4.4% , which is an
686 improvement compared to the NMB of -14.7% in the standard simulation.
687 However, the increases in SO_2 emissions lead to larger NMBs of surface-layer
688 NO_3^- and NH_4^+ because of the increased formation of ammonium sulfate or
689 ammonium bisulfate. The percentage contributions of SO_4^{2-} to total aerosol
690 mass in the UTLS increase slightly by 2.7% at 200 hPa and by 1.6% at 100
691 hPa, and nitrate in the UTLS also shows small sensitivity to the change in SO_2
692 emissions.

693 With anthropogenic emissions of NO_x in Asia reduced by 50%, the NMB of
694 simulated surface-layer NO_3^- concentrations changes from $+51.5\%$ in the
695 standard simulation to -11.7% in this sensitivity run. The contribution of each
696 of SO_4^{2-} , NO_3^- and NH_4^+ aerosols to total aerosol mass in the UTLS is not
697 sensitive to this reduction in NO_x emissions at the surface; the percentage

698 contribution obtained from this sensitivity run is very close to the value
699 obtained in the standard simulation (Table 4). Similarly, in the sensitivity study
700 with NH₃ emissions reduced by 50% in Asia, simulated surface-layer
701 concentrations of NO₃⁻ and NH₄⁺ are improved in terms of the values of NMBs,
702 but the improvement in simulated aerosol concentrations at the surface-layer
703 does not influence our conclusion of high nitrate aerosol concentration in the
704 UTLS.

705 As shown in Table 4, for the surface layer, simulated nitrate concentration
706 over the TP/SASM region decreases by 46.8% with a 50% reduction in
707 anthropogenic NO_x emissions in Asia, and it decreases by 22.3% when
708 anthropogenic NH₃ emissions are reduced by the same percentage, indicating
709 that surface-layer nitrate aerosol is more sensitive to anthropogenic emissions
710 of NO_x than to those of NH₃. Relative to the baseline simulation, simulated
711 nitrate concentrations at 200 hPa and 100 hPa decrease, respectively, by 49.0%
712 and 17.7% with a 50% reduction in NH₃ emissions, whereas only by 2.1% and
713 1.3% with a 50% reduction in NO_x emissions. Over the studied region, the role
714 of NH₃ in the sulfate-nitrate-ammonium aerosol system can be quantified by
715 the gas ratio of $GR = \frac{\text{free ammonia}}{\text{total nitrate}} = \frac{TA - 2 \times TS}{TN}$ (Ansari and Pandis, 1998), where
716 $TA = \text{NH}_3 + \text{NH}_4^+$, $TS = \text{SO}_4^{2-}$, and $TN = \text{HNO}_3 + \text{NO}_3^-$. Over the TP/SASM
717 region, GR is generally positive both at the surface and in the UTLS, especially
718 over 20–40°N where deep convection exits (Fig. 11), indicating that S(VI) is in
719 the form of sulfate and free ammonia is available to react with nitrate (Seinfeld
720 and Pandis 2006). However, GR is generally less than 1.0 above 400 hPa in
721 summer over the TP/SASM region, which indicates nitrate concentrations are
722 most sensitive to changes in NH₃ and explains the small sensitivity of nitrate

723 aerosol to NO_x emissions in the UTLS.

724 In the sensitivity study with emissions of NO_x , NH_3 , and SO_2 in Asia
725 changed simultaneously, simulated surface-layer concentrations of SO_4^{2-} , NO_3^-
726 and NH_4^+ have NMBs of -8.3% , -27.0% and $+55.4\%$, respectively, which are
727 all improved compared to those in the standard simulation. Even though nitrate
728 aerosol is now underestimated at the surface, it still accounts for 53.3% of the
729 $\text{PM}_{2.5}$ concentration at 100 hPa over the TP/SASM region in summer.

730 It should be noted that the concentrations of OC and BC are also
731 underestimated, with NMBs of -57.2% and -32.2% , respectively, in summer
732 (Section 4.2). We have done a simple calculation with the concentrations of
733 OC and BC in the UTLS multiplied by 2.3 and 1.5, respectively, and nitrate is
734 still the most dominant aerosol species in summertime in the UTLS over the
735 TP/SASM region (not shown in Table 4). Therefore the uncertainties in surface
736 aerosol concentrations do not compromise the conclusion of this study.

737

738 **8 Conclusions**

739 In this work we simulate nitrate aerosol and its contribution to aerosol
740 concentrations in the UTLS over the TP/SASM region ($70\text{--}105^\circ\text{E}$, $10\text{--}40^\circ\text{N}$)
741 for summertime of year 2005, using the global chemical transport model
742 GEOS-Chem driven by the assimilated meteorological fields.

743 Simulated HNO_3 and O_3 are evaluated to show the model's ability to
744 simulate the $\text{NO}_x\text{-O}_3\text{-HNO}_3$ cycle over the studied region. In the UTLS, both
745 the horizontal and vertical distributions of simulated HNO_3 and O_3 agree well
746 with the MLS observations. At 100 hPa, simulated seasonal mean HNO_3 and
747 O_3 mixing ratios show NMBs of $+11.1\%$ and $+3.5\%$, respectively, over the

748 TP/SASM region (70–105°E, 10–40°N) in summer of year 2005, and the model
749 biases lie within the confidence range of the MLS instruments. Both simulated
750 and observed O₃ concentrations show relatively low values of less than 200
751 ppbv at 100 hPa over the TP/SASM region.

752 Averaged over the TP/SASM region, the surface-layer concentrations of
753 SO₄²⁻, NO₃⁻, NH₄⁺, BC, and OC are simulated to be 1.70, 0.94, 0.85, 0.30, and
754 0.94 μg m⁻³, respectively. Nitrate aerosol is simulated to be of secondary
755 importance near the surface over the region of our interest. Comparisons of
756 simulated aerosol concentrations with ground-based observations show that
757 simulated summertime concentrations of SO₄²⁻, NO₃⁻, NH₄⁺, OC and BC have
758 NMB of -14.7%, +51.5%, +74.9%, -57.2% and -32.2%, respectively. Note that
759 the measurements of NO₃⁻ and NH₄⁺ are quite limited in terms of the number
760 of samples.

761 Model results show elevated concentrations of SO₄²⁻, NO₃⁻, NH₄⁺, OC, BC
762 and PM_{2.5} in the UTLS over the TP/SASM region throughout the summer. NO₃⁻
763 is simulated to be the most dominant aerosol species in the UTLS of the
764 TP/SASM region. Accounting for NO₃⁻ aerosol, the GEOS-Chem model
765 reproduces well the magnitude of aerosol extinctions above 10 km, as model
766 results are compared with the SAGE II measurements. The discrepancies
767 between the simulated and observed aerosol extinction coefficient are within 8%
768 in the UTLS (averaged over 14–16 km). Simulated vertical profiles of aerosol
769 extinction coefficients with and without nitrate aerosol show large
770 discrepancies from 6 km to tropopause, indicating the important role of nitrate
771 in aerosol layer in the UTLS over the TP/SASM region.

772 The contribution of NO₃⁻ to aerosols in the TP/SASM region is quantified

773 by C_{NIT} (the ratio of nitrate concentration to $\text{PM}_{2.5}$ concentration). Over the
774 TP/SASM region, the C_{NIT} values in summer are 5–35% at the surface, 25–
775 50% at 200 hPa, and could exceed 60% at 100 hPa. The mechanisms for the
776 accumulation of nitrate in the UTLS over the TP/SASM region include vertical
777 transport and the gas-to-aerosol conversion of HNO_3 to form nitrate. Such
778 gas-to-aerosol conversion occurs during the upward transport and in the UTLS.
779 The high relative humidity and low temperature associated with the deep
780 convection over the TP/SASM region are favorable for nitrate formation.

781 Results from the present study indicate that nitrate is an important aerosol
782 species in the UTLS over the TP/SASM region. Considering the scarce
783 measurements of nitrate in the UTLS and the model uncertainties, more
784 observational and modeling studies are needed to further explore the aerosol
785 composition in the Asian tropopause aerosol layer. Further simulations of
786 nitrate aerosol in the UTLS also need to account for NAT formation at low
787 temperatures (Kirner et al., 2011) and the roles of natural aerosols, including
788 the transport of mineral dust and sea salt to the UTLS as well as nitrate
789 formation on these natural particles (Ma et al., 2003).

790

791

792 *Acknowledgments.* This work was supported by the National Basic Research
793 Program of China (973 program, Grant No. 2014CB441202), the Strategic
794 Priority Research Program of the Chinese Academy of Sciences (Grant No.
795 XDA05100503), and the National Natural Science Foundation of China under
796 grants 41021004, 41475137, and 91544219. We gratefully acknowledge
797 NASA, USA, for providing the MLS and SAGE II data on their website.

799 **References**

- 800 Ansari, A. S., and Pandis, S. N.: Response of Inorganic PM to Precursor
801 Concentrations, *Environ. Sci. Technol.*, 32(18), 2706–2714, 1998.
- 802 Adhikary, B., Carmichael, G. R., Tang, Y., Leung, L. R., Qian, Y., Schauer, J. J.,
803 Stone, E. A., Ramanathan, V., and Ramana, M. V.: Characterization of the
804 seasonal cycle of south Asian aerosols: A regional-scale modeling
805 analysis, *J. Geophys. Res.*, 112, D22S22, doi:10.1029/2006JD008143,
806 2007.
- 807 Alexander, B., Park, R. J., Jacob, D. J., Li, Q., Yantosca, R. M., Savarino, J.,
808 Lee, C., and Thiemens, M.: Sulfate formation in sea-salt aerosols:
809 Constraints from oxygen isotopes, *J. Geophys. Res.*, 110, D10307,
810 doi:10.1029/2004JD005659, 2005.
- 811 Arimoto, R., Duce, R., Savoie, D., Prospero, J., Talbot, R., Cullen, J., Tomza,
812 U., Lewis, N., and Ray, B.: Relationships among aerosol constituents from
813 Asia and the North Pacific during PEM–West A, *J. Geophys. Res.*, 101,
814 2011–2023, 1996.
- 815 Babu, S. S. and Moorthy, K. K.: Aerosol black carbon over a tropical coastal
816 station in India, *Geophys. Res. Lett.*, 29, 2098,
817 doi:10.1029/2002GL015662, 2002.
- 818 Bano, T., Singh, S., Gupta, N., Soni, K., Tanwar, R., Nath, S., Arya, B., and
819 Gera, B.: Variation in aerosol black carbon concentration and its emission
820 estimates at the mega-city Delhi, *Int. J. Remote Sens.*, 32, 6749–6764,
821 2011.
- 822 Bian, J., Yan, R., and Chen, H.: Tropospheric Pollutant Transport to the
823 Stratosphere by Asian Summer Monsoon, *Chinese Journal of*
824 *Atmospheric Sciences*, 35, 897–902, 2011a.
- 825 Bian, J., Yan, R., Chen, H., Lü, D., and MASSIE, S. T.: Formation of the
826 Summertime Ozone Valley over the Tibetan Plateau: The Asian Summer
827 Monsoon and Air Column Variations, *Adv. Atmos. Sci.*, 28, 1318–1325,
828 2011b.
- 829 Bian, J., Pan, L. L., Paulik, L., Vömel, H., Chen, H., and Lü, D.: In situ water
830 vapor and ozone measurements in Lhasa and Kunming during the Asian
831 summer monsoon, *Geophys. Res. Lett.*, 39, L19808,
832 doi:10.1029/2012GL052996, 2012.
- 833 Bourgeois, Q., Bey, I., and Stier, P.: A permanent aerosol layer at the tropical
834 tropopause layer driven by the intertropical convergence zone, *Atmos.*
835 *Chem. Phys. Discuss.*, 12, 2863–2889, 2012.
- 836 Bouwman, A., Lee, D., Asman, W., Dentener, F., Van Der Hoek, K., and Olivier,
837 J.: A global high-resolution emission inventory for ammonia, *Global*
838 *Biogeochem. Cy.*, 11, 561–587, 1997.
- 839 Brewer, A. W.: Evidence for a world circulation provided by the measurements
840 of helium and water vapour distribution in the stratosphere, *Q. J. Roy.*
841 *Meteor. Soc.*, 75, 351–363, 1949.
- 842 Carrico, C. M., Bergin, M. H., Shrestha, A. B., Dibb, J. E., Gomes, L., and
843 Harris, J. M.: The importance of carbon and mineral dust to seasonal
844 aerosol properties in the Nepal Himalaya, *Atmos. Environ.*, 37, 2811–2824,
845 2003.

846 Carslaw, K., Wirth, M., Tsias, A., Luo, B., Dörnbrack, A., Leutbecher, M.,
847 Volkert, H., Renger, W., Bacmeister, J., and Peter, T.: Particle
848 microphysics and chemistry in remotely observed mountain polar
849 stratospheric clouds, *J. Geophys. Res.*, 103, 5785–5796, 1998.

850 Chatterjee, A., Adak, A., Singh, A. K., Srivastava, M. K., Ghosh, S. K., Tiwari,
851 S., Devara, P. C., and Raha, S.: Aerosol chemistry over a high altitude
852 station at northeastern Himalayas, India, *PloS one*, 5, e11122,
853 doi:10.1371/journal.pone.0011122, 2010.

854 Chatterjee, A., Ghosh, S. K., Adak, A., Singh, A. K., Devara, P. C., and Raha,
855 S.: Effect of Dust and Anthropogenic Aerosols on Columnar Aerosol
856 Optical Properties over Darjeeling (2200 m asl), Eastern Himalayas, India,
857 *PloS one*, 7, e40286, doi:10.1371/journal.pone.0040286, 2012.

858 Chen, H., Bian, J., and Lü, D.: Advances and prospects in the study of
859 stratosphere-troposphere exchange, *Chinese J. Atmos. Sci.*, 30, 813–820,
860 doi:1006-9895(2006)30:5<813:SDLCXP>2.0.TX;2-A, 2006.

861 Chin, M., Ginoux, P., Kinne, S., Torres, O., Holben, B., Duncan, B. N., Martin,
862 R. V., Logan, J. A., Higurashi, A., and Nakajima, T.: Tropospheric aerosol
863 optical thickness from the GOCART model and comparisons with satellite
864 and sunphotometer measurements, *J. Atmos. Sci.*, 59, 461–483, 2002.

865 Chowdhury, Z., Zheng, M., Schauer, J. J., Sheesley, R. J., Salmon, L. G., Cass,
866 G. R., and Russell, A. G.: Speciation of ambient fine organic carbon
867 particles and source apportionment of PM_{2.5} in Indian cities, *J. Geophys.*
868 *Res.*, 112, D15303, doi:10.1029/2007JD008386, 2007.

869 Chu, W., McCormick, M., Lenoble, J., Brogniez, C., and Pruvost, P.: SAGE II
870 inversion algorithm, *J. Geophys. Res.*, 94, 8339–8351, 1989.

871 Chung, S. H., and Seinfeld, J. H.: Global distribution and climate forcing of
872 carbonaceous aerosols, *J. Geophys. Res.*, 107(D19), 4407,
873 doi:10.1029/2001JD001397, 2002.

874 Collins, W. J., Stevenson, D. S., Johnson, C. E., and Derwent, R. G.: The
875 European regional ozone distribution and its links with the global scale for
876 the years 1992 and 2015, *Atmos. Environ.*, 34, 255–267, 2000.

877 Considine, D. B., Rosenfield, J. E., and Fleming, E. L.: An interactive model
878 study of the influence of the Mount Pinatubo aerosol on stratospheric
879 methane and water trends, *J. Geophys. Res.*, 106, 27711-27727,
880 doi:10.1029/2001jd000331, 2001.

881 Considine, D. B., Logan, J. A., and Olsen, M. A.: Evaluation of
882 near-tropopause ozone distributions in the Global Modeling Initiative
883 combined stratosphere/troposphere model with ozonesonde data, *Atmos.*
884 *Chem. Phys.*, 8, 2365–2385, 2008.

885 Cooke, W. F., Liousse, C., Cachier, H., and Feichter, J.: Construction of a 1°x1°
886 fossil fuel emission data set for carbonaceous aerosol and implementation
887 and radiative impact in the ECHAM-4 model, *J. Geophys. Res.*, 104,
888 22,137–22,162, 1999.

889 Datta, A., Sharma, S., Harit, R., Kumar, V., Mandal, T., and Pathak, H.:
890 Ammonia emission from subtropical crop land area in India, *Asia-Pac. J.*
891 *Atmos. Sci.*, 48, 275–281, 2012.

892 Dawson, J., Adams, P., and Pandis, S.: Sensitivity of PM_{2.5} to climate in the
893 Eastern US: a modeling case study, *Atmos. Chem. and phys.*, 7, 4295–
894 4309, 2007.

895 Decesari, S., Facchini, M., Carbone, C., Giulianelli, L., Rinaldi, M., Finessi, E.,

896 Fuzzi, S., Marinoni, A., Cristofanelli, P., and Duchi, R.: Chemical
897 composition of PM₁₀ and PM₁ at the highaltitude Himalayan station Nepal
898 Climate Observatory-Pyramid (NCO-P)(5079 m asl), *Atmos. Chem. Phys.*,
899 10, 4583–4596, 2010.

900 Dobson, G. M. B.: Origin and distribution of the polyatomic molecules in the
901 atmosphere, *Proceedings of the Royal Society of London. Series A,*
902 *Mathematical and Physical Sciences*, 187–193, 1956.

903 Drury, E., Jacob, D. J., Spurr, R. J., Wang, J., Shinozuka, Y., Anderson, B. E.,
904 Clarke, A. D., Dibb, J., McNaughton, C., and Weber, R.: Synthesis of
905 satellite (MODIS), aircraft (ICARTT), and surface (IMPROVE, EPA–AQS,
906 AERONET) aerosol observations over eastern North America to improve
907 MODIS aerosol retrievals and constrain surface aerosol concentrations
908 and sources, *J. Geophys. Res.*, 115, D14204, doi:10.1029/2009JD012629,
909 2010.

910 Duncan, B., Strahan, S., Yoshida, Y., Steenrod, S., and Livesey, N.: Model
911 study of the cross-tropopause transport of biomass burning pollution,
912 *Atmos. Chem. Phys.*, 7, 3713–3736, 2007.

913 Dutkiewicz, V. A., Alvi, S., Ghauri, B. M., Choudhary, M. I., and Husain, L.:
914 Black carbon aerosols in urban air in South Asia, *Atmos. Environ.*, 43,
915 1737–1744, 2009.

916 Evans, M., and Jacob, D. J.: Impact of new laboratory studies of N₂O₅
917 hydrolysis on global model budgets of tropospheric nitrogen oxides, ozone,
918 and OH, *Geophys. Res. Lett.*, 32, 10 L09813, doi:10.1029/2005GL022469,
919 2005.

920 Fadnavis, S., Semeniuk, K., Pozzoli, L., Schultz, M., Ghude, S., Das, S., and
921 Kakatkar, R.: Transport of aerosols into the UTLS and their impact on the
922 Asian monsoon region as seen in a global model simulation, *Atmos. Chem.*
923 *Phys.*, 13, 8771–8786, 2013.

924 Fadnavis, S., Semeniuk, K., Schultz, M., Mahajan, A., Pozzoli, L., Sonbawane,
925 S., and Kiefer, M.: Transport pathways of peroxyacetyl nitrate in the upper
926 troposphere and lower stratosphere from different monsoon systems
927 during the summer monsoon season, *Atmos. Chem. Phys. Discuss.*, 14,
928 20159–20195, 2014.

929 Fairlie, T. D., Jacob, D. J., and Park, R. J.: The impact of transpacific transport
930 of mineral dust in the United States, *Atmos. Environ.*, 41, 1251–1266,
931 2007.

932 Fisher, J. A., Jacob, D. J., Wang, Q., Bahreini, R., Carouge, C. C., Cubison, M.
933 J., Dibb, J. E., Diehl, T., Jimenez, J. L., and Leibensperger, E. M.: Sources,
934 distribution, and acidity of sulfate–ammonium aerosol in the Arctic in
935 winter–spring, *Atmos. Environ.*, 45, 7301–7318, 2011.

936 Fountoukis, C., and Nenes, A.: ISORROPIA II: a computationally efficient
937 thermodynamic equilibrium model for K⁺–Ca²⁺–Mg²⁺–NH₄⁺–Na⁺–SO₄²⁻–
938 NO₃⁻–Cl⁻–H₂O aerosols, *Atmos. Chem. Phys.*, 7, 4639–4659, 2007.

939 Froyd, K., Murphy, D., Sanford, T., Thomson, D., Wilson, J., Pfister, L., and Lait,
940 L.: Aerosol composition of the tropical upper troposphere, *Atmos. Chem.*
941 *Phys.*, 9, 4363–4385, 2009.

942 Fu, R., Hu, Y., Wright, J. S., Jiang, J. H., Dickinson, R. E., Chen, M., Filipiak,
943 M., Read, W. G., Waters, J. W., and Wu, D. L.: Short circuit of water vapor
944 and polluted air to the global stratosphere by convective transport over the
945 Tibetan Plateau, *P. Natl. A. Sci.*, 103, 5664–5669, 2006.

946 Fu, T. -M., Cao, J., Zhang, X., Lee, S., Zhang, Q., Han, Y., Qu, W., Han, Z.,
947 Zhang, R., and Wang, Y.: Carbonaceous aerosols in China: top-down
948 constraints on primary sources and estimation of secondary contribution,
949 *Atmos. Chem. Phys.*, 12, 2725–2746, 2012.

950 Ganguly, D., Jayaraman, A., and Gadhavi, H.: Physical and optical properties
951 of aerosols over an urban location in western India: Seasonal variabilities,
952 *J. Geophys. Res.*, 111, D24206, doi:10.1029/2006JD007392, 2006.

953 George, S. K., and Nair, P. R.: Aerosol mass loading over the marine
954 environment of Arabian Sea during ICARB: Sea-salt and non-sea-salt
955 components, *J. Earth Syst. Sci.*, 117, 333–344, 2008.

956 George, S. K., Nair, P. R., Parameswaran, K., Jacob, S., and Abraham, A.:
957 Seasonal trends in chemical composition of aerosols at a tropical coastal
958 site of India, *J. Geophys. Res.*, 113, D16209, doi:10.1029/2007JD009507,
959 2008.

960 Gettelman, A., Kinnison, D. E., Dunkerton, T. J., and Brasseur, G. P.: Impact of
961 monsoon circulations on the upper troposphere and lower stratosphere, *J.*
962 *Geophys. Res.*, 109, D22101, doi:10.1029/2004JD004878, 2004.

963 Guenther, A., Karl, T., Harley, P., Wiedinmyer, C., Palmer, P., and Geron, C.:
964 Estimates of global terrestrial isoprene emissions using MEGAN (Model of
965 Emissions of Gases and Aerosols from Nature), *Atmos. Chem. Phys.*
966 *Discuss.*, 6, 107–173, 2006.

967 Hack, J. J.: Parameterization of moist convection in the National Center for
968 Atmospheric Research community climate model (CCM2), *J. Geophys.*
969 *Res.*, 99, 5551–5568, doi:10.1029/93jd03478, 1994.

970 He, Q., Li, C., Ma, J., Wang, H., Yan, X., Liang, Z., and Qi, G.: Enhancement of
971 aerosols in UTLS over the Tibetan Plateau induced by deep convection
972 during the Asian summer monsoon, *Atmos. Chem. Phys. Discuss.*, 14,
973 3169–3191, 10.5194/acpd-14-3169-2014, 2014.

974 Hegde, P., Sudheer, A., Sarin, M., and Manjunatha, B.: Chemical
975 characteristics of atmospheric aerosols over southwest coast of India,
976 *Atmos. Environ.*, 41, 7751–7766, 2007.

977 Hofmann, D., Rosen, J., Harder, J., and Hereford, J.: Balloon-borne
978 measurements of aerosol, condensation nuclei, and cloud particles in the
979 stratosphere at McMurdo Station, Antarctica, during the spring of 1987, *J.*
980 *Geophys. Res.*, 94, 11253–11269, doi:10.1029/JD094iD09p11253, 1989.

981 Huang, C., Chen, C. H., Li, L., Cheng, Z., Wang, H. L., Huang, H. Y., Streets, D.
982 G., and Wang, Y. J.: Emission inventory of anthropogenic air pollutants
983 and VOC species in the Yangtze River Delta region, China, *Atmos. Chem.*
984 *Phys.*, 11, 4105–4120, 2011.

985 Huang, X., Song, Y., Li, M., Li, J., Huo, Q., Cai, X., Zhu, T., Hu, M., and Zhang,
986 H.: A high-resolution ammonia emission inventory in China, *Global*
987 *Biogeochem. Cy.*, 26, GB1030, doi:10.1029/2011GB004161, 2012.

988 Husain, L., Dutkiewicz, V. A., Khan, A., and Ghauri, B. M.: Characterization of
989 carbonaceous aerosols in urban air, *Atmos. Environ.*, 41, 6872–6883,
990 2007.

991 Jacob, D. J.: Heterogeneous chemistry and tropospheric ozone, *Atmos.*
992 *Environ.*, 34, 2131–2159, 2000.

993 Jaeglé, L., Quinn, P., Bates, T., Alexander, B., and Lin, J.-T.: Global distribution
994 of sea salt aerosols: new constraints from in situ and remote sensing
995 observations, *Atmos. Chem. Phys.*, 11, 3137–3157, 2011.

996 Jayaraman, A., Gadhavi, H., Ganguly, D., Misra, A., Ramachandran, S., and
997 Rajesh, T.: Spatial variations in aerosol characteristics and regional
998 radiative forcing over India: Measurements and modeling of 2004 road
999 campaign experiment, *Atmos. Environ.*, 40, 6504–6515, 2006.

1000 Jeong, J. I., and Park, R. J.: Effects of the meteorological variability on regional
1001 air quality in East Asia, *Atmos. Environ.*, 69, 46–55, 2013.

1002 Jiang, H., Liao, H., Pye, H., Wu, S., Mickley, L. J., Seinfeld, J. H., and Zhang,
1003 X.: Projected effect of 2000-2050 changes in climate and emissions on
1004 aerosol levels in China and associated transboundary transport, *Atmos.*
1005 *Chem. Phys.*, 13, 7937–7960, 2013.

1006 Kar, J., Bremer, H., Drummond, J. R., Rochon, Y. J., Jones, D., Nichitiu, F., Zou,
1007 J., Liu, J., Gille, J. C., and Edwards, D. P.: Evidence of vertical transport of
1008 carbon monoxide from Measurements of Pollution in the Troposphere
1009 (MOPITT), *Geophys. Res. Lett.*, 31, L23105, doi:10.1029/2004GL021128,
1010 2004.

1011 Kim, J., Song, C. H., Ghim, Y., Won, J., Yoon, S., Carmichael, G., and Woo, J.
1012 H.: An investigation on NH₃ emissions and particulate NH₄⁺ – NO₃⁻
1013 formation in East Asia, *Atmos. Environ.*, 40, 2139–2150, 2006.

1014 Kim, Y.- S., Shibata, T., Iwasaka, Y., Shi, G., Zhou, X., Tamura, K., and Ohashi,
1015 T.: Enhancement of aerosols near the cold tropopause in summer over
1016 Tibetan Plateau: lidar and balloonborne measurements in 1999 at Lhasa,
1017 Tibet, China, in: *Lidar Remote Sensing for Industry and Environment*
1018 *Monitoring III*, edited by: Singh U. N., Itabe, T., and Liu, Z., Proceedings of
1019 SPIE, Hangzhou, China, 4893, 496–503, 2003.

1020 Kirner, O., Ruhnke, R., Buchholz-Dietsch, J., Jöckel, P., Brühl, C., and Steil, B.:
1021 Simulation of polar stratospheric clouds in the chemistry-climate-model
1022 EMAC via the submodel PSC, *Geoscientific Model Development*, 4, 169–
1023 182, 2011.

1024 Kulkarni, P., and Ramachandran, S.: Comparison of aerosol extinction
1025 between lidar and SAGE II over Gadanki, a tropical station in India, *Ann.*
1026 *Geophys.*, 33, 3, 351–362, 2015.

1027 Kulshrestha, U., Saxena, A., Kumar, N., Kumari, K., and Srivastava, S.:
1028 Chemical composition and association of size-differentiated aerosols at a
1029 suburban site in a semi-arid tract of India, *J. Atmos. Chem.*, 29, 109–118,
1030 1998.

1031 Latha, K. M., and Badarinath, K.: Seasonal variations of black carbon aerosols
1032 and total aerosol mass concentrations over urban environment in India,
1033 *Atmos. Environ.*, 39, 4129–4141, 2005.

1034 Lau, K. M., Kim, M. K., and Kim, K. M.: Asian summer monsoon anomalies
1035 induced by aerosol direct forcing: the role of the Tibetan Plateau, *Clim.*
1036 *Dyn.*, 26, 855–864, doi:10.1007/s00382-006-0114-z, 2006.

1037 Lawrence, M. G., and Lelieveld, J.: Atmospheric pollutant outflow from
1038 southern Asia: a review, *Atmos. Chem. Phys.*, 10, 11017-11096,
1039 doi:10.5194/acp-10-11017-2010, 2010.

1040 Lelieveld, J., Crutzen, P. J., Ramanathan, V., Andreae, M. O., Brenninkmeijer,
1041 C. A. M., Campos, T., Cass, G. R., Dickerson, R. R., Fischer, H., de Gouw,
1042 J. A., Hansel, A., Jefferson, A., Kley, D., de Laat, A. T. J., Lal, S., Lawrence,
1043 M. G., Lobert, J. M., Mayol-Bracero, O. L., Mitra, A. P., Novakov, T.,
1044 Oltmans, S. J., Prather, K. A., Reiner, T., Rodhe, H., Scheeren, H. A.,
1045 Sikka, D., and Williams, J.: The Indian Ocean Experiment: Widespread air

1046 pollution from South and Southeast Asia, *Science*, 291, 1031–1036,
1047 doi:10.1126/science.1057103, 2001.

1048 Leon, J.-F., Chazette, P., Dulac, F., Pelon, J., Flamant, C., Bonazzola, M.,
1049 Foret, G., Alfaro, S., Cachier, H., and Cautenet, S.: Large-scale advection
1050 of continental aerosols during INDOEX, *J. Geophys. Res.*, 106, 28427–
1051 28428, 28439, 2001.

1052 Li, Q., Jiang, J. H., Wu, D. L., Read, W. G., Livesey, N. J., Waters, J. W., Zhang,
1053 Y., Wang, B., Filipiak, M. J., and Davis, C. P.: Convective outflow of South
1054 Asian pollution: A global CTM simulation compared with EOS MLS
1055 observations, *Geophys. Res. Lett.*, 32, L14826,
1056 doi:10.1029/2005GL022762, 2005.

1057 Liao, H., Adams, P. J., Chung, S. H., Seinfeld, J. H., Mickley, L. J., and Jacob,
1058 D. J.: Interactions between tropospheric chemistry and aerosols in a
1059 unified general circulation model, *J. Geophys. Res.*, 108, 4001,
1060 doi:10.1029/2001JD001260, 2003.

1061 Liao, H., and Seinfeld, J. H.: Global impacts of gas-phase chemistry-aerosol
1062 interactions on direct radiative forcing by anthropogenic aerosols and
1063 ozone, *J. Geophys. Res.*, 110, D18208, doi:10.1029/2005JD005907,
1064 2005.

1065 Liao, H., Zhang, Y., Chen, W.-T., Raes, F., and Seinfeld, J. H.: Effect of
1066 chemistry-aerosol-climate coupling on predictions of future climate and
1067 future levels of tropospheric ozone and aerosols, *J. Geophys. Res.*, 114,
1068 D10306, doi:10.1029/2008JD010984, 2009.

1069 Liu, H., Jacob, D. J., Bey, I., and Yantosca, R. M.: Constraints from ²¹⁰Pb and
1070 ⁷Be on wet deposition and transport in a global three-dimensional
1071 chemical tracer model driven by assimilated meteorological fields, *J.*
1072 *Geophys. Res.*, 106, 12109–12128, 2001.

1073 Liu, X., Penner, J. E., and Wang, M.: Influence of anthropogenic sulfate and
1074 black carbon on upper tropospheric clouds in the NCAR CAM3 model
1075 coupled to the IMPACT global aerosol model, *J. Geophys. Res.*, 114,
1076 D03204, doi:10.1029/2008JD010492, 2009.

1077 Livesey, N. J., Filipiak, M. J., Froidevaux, L., Read, W. G., Lambert, A., Santee,
1078 M. L., Jiang, J. H., Pumphrey, H. C., Waters, J. W., and Cofield, R. E.:
1079 Validation of Aura Microwave Limb Sounder O₃ and CO observations in
1080 the upper troposphere and lower stratosphere, *J. Geophys. Res.*, 113,
1081 D15S02, doi:10.1029/2007JD008805, 2008.

1082 Livesey, N. J., Read, W. G., Wagner, P. A., Froidevaux, L., Lambert, A.,
1083 Manney, G. L., Pumphrey, H. C., Santee, M. L., Schwartz, M. J., Wang, S.,
1084 Cofield, R. E., Cuddy, D. T., Fuller, R. A., Jarnot, R. F., Jiang, J. H., and
1085 Knosp, B. W.: Version 3.3 Level 2 data quality and description document,
1086 JPL D-33509, 2011.

1087 Lodhi, A., Ghauri, B., Khan, M. R., Rahman, S., and Shafique, S.: Particulate
1088 matter (PM_{2.5}) concentration and source apportionment in Lahore, *J.*
1089 *Brazil. Chem. Soc.*, 20, 1811–1820, 2009.

1090 Lou, S., Liao, H., and Zhu, B.: Impacts of aerosols on surface-layer ozone
1091 concentrations in China through heterogeneous reactions and changes in
1092 photolysis rates, *Atmos. Environ.*, 85, 123–138, 2014.

1093 Luo, Y., Zhang, R., Qian, W., Luo, Z., and Hu, X.: Inter-comparison of deep
1094 convection over the Tibetan Plateau–Asian monsoon region and
1095 subtropical North America in boreal summer using CloudSat/CALIPSO

1096 data, *Journal of Climate*, 24(8), 2164–2177, 2011.

1097 Ma, J., Tang, J., Li, S.-M., and Jacobson, M. Z.: Size distributions of ionic
1098 aerosols measured at Waliguan Observatory: Implication for nitrate
1099 gas-to-particle transfer processes in the free troposphere, *J. Geophys.*
1100 *Res.*, 108, 4541, doi:10.1029/2002jd003356, 2003.

1101 Martin, R. V., Jacob, D. J., Yantosca, R. M., Chin, M., and Ginoux, P.: Global
1102 and regional decreases in tropospheric oxidants from photochemical
1103 effects of aerosols, *J. Geophys. Res.*, 108, 4097,
1104 doi:10.1029/2002JD002622, 2003.

1105 McCormick, M. P.: SAGE II: an overview, *Adv. Space Res.*, 7, 219-226, 1987.

1106 McLinden, C., Olsen, S., Hannegan, B., Wild, O., Prather, M., and Sundet, J.:
1107 Stratospheric ozone in 3-D models: A simple chemistry and the
1108 cross-tropopause flux, *J. Geophys. Res.*, 105, 14653–14665,
1109 doi:10.1029/2000JD900124, 2000.

1110 Mickley, L. J., Murti, P., Jacob, D. J., Logan, J. A., Koch, D., and Rind, D.:
1111 Radiative forcing from tropospheric ozone calculated with a unified
1112 chemistry-climate model, *J. Geophys. Res.*, 104, 30153-30172, 1999.

1113 Ming, J., Zhang, D., Kang, S., and Tian, W.: Aerosol and fresh snow chemistry
1114 in the East Rongbuk Glacier on the northern slope of Mt. Qomolangma
1115 (Everest), *J. Geophys. Res.*, 112, D15307, doi:10.1029/2007JD008618,
1116 2007.

1117 Momin, G. A., Rao, P. S. P., Safai, P. D., Ali, K., Naik, M. S., and Pillai, A. G.:
1118 Atmospheric aerosol characteristic studies at Pune and
1119 Thiruvananthapuram during INDOEX programme–1998, *Curr. Sci.*, 76,
1120 985-989, 1999.

1121 Mu, Q., and Liao, H.: Simulation of the interannual variations of aerosols in
1122 China: role of variations in meteorological parameters, *Atmos. Chem.*
1123 *Phys.*, 14, 9597–9612, 2014.

1124 Murray, L. T., Jacob, D. J., Logan, J. A., Hudman, R. C., and Koshak, W. J.:
1125 Optimized regional and interannual variability of lightning in a global
1126 chemical transport model constrained by LIS/OTD satellite data, *J.*
1127 *Geophys. Res.*, 117, D20307, doi:10.1029/2012JD017934, 2012.

1128 Nair, P. R., George, S. K., Sunilkumar, S., Parameswaran, K., Jacob, S., and
1129 Abraham, A.: Chemical composition of aerosols over peninsular India
1130 during winter, *Atmos. Environ.*, 40, 6477–6493, 2006.

1131 Nair, V. S., Solmon, F., Giorgi, F., Mariotti, L., Babu, S. S., and Moorthy, K. K.:
1132 Simulation of South Asian aerosols for regional climate studies, *J.*
1133 *Geophys. Res.*, 117, D04209, doi:10.1029/2011JD016711, 2012.

1134 Nakamura, T., Matsumoto, K., and Uematsu, M.: Chemical characteristics of
1135 aerosols transported from Asia to the East China Sea: an evaluation of
1136 anthropogenic combined nitrogen deposition in autumn, *Atmos. Environ.*,
1137 39, 1749–1758, 2005.

1138 Oberbeck, V. R., Livingston, J. M., Russell, P. B., Pueschel, R. F., Rosen, J. N.,
1139 Osborn, M. T., Kritiz, M. A., Snetsinger, K. G., and Ferry, G. V.: SAGE II
1140 aerosol validation: Selected altitude measurements, including particle
1141 micrometeorology, *J. Geophys. Res.*, 94, 8367–8380,
1142 doi:10.1029/JD094iD06p08367, 1989.

1143 Pant, P., Hegde, P., Dumka, U., Sagar, R., Satheesh, S., Moorthy, K. K., Saha,
1144 A., and Srivastava, M.: Aerosol characteristics at a high-altitude location in
1145 central Himalayas: Optical properties and radiative forcing, *J. Geophys.*

1146 Res., 111, D17206, doi:10.1029/2005JD006768, 2006.
 1147 Park, M., Randel, W. J., Kinnison, D. E., Garcia, R. R., and Choi, W.: Seasonal
 1148 variation of methane, water vapor, and nitrogen oxides near the
 1149 tropopause: Satellite observations and model simulations, *J. Geophys.*
 1150 *Res.*, 109, D03302, doi:10.1029/2003JD003706, 2004.
 1151 Park, M., Randel, W. J., Gettelman, A., Massie, S. T., and Jiang, J. H.:
 1152 Transport above the Asian summer monsoon anticyclone inferred from
 1153 Aura Microwave Limb Sounder tracers, *J. Geophys. Res.*, 112, D16309,
 1154 doi:10.1029/2006JD008294, 2007.
 1155 Park, M., Randel, W. J., Emmons, L. K., Bernath, P. F., Walker, K. A., and
 1156 Boone, C. D.: Chemical isolation in the Asian monsoon anticyclone
 1157 observed in Atmospheric Chemistry Experiment (ACE-FTS) data, *Atmos.*
 1158 *Chem. Phys.*, 8, 757–764, 2008.
 1159 Park, M., Randel, W. J., Emmons, L. K., and Livesey, N. J.: Transport
 1160 pathways of carbon monoxide in the Asian summer monsoon diagnosed
 1161 from Model of Ozone and Related Tracers (MOZART), *J. Geophys. Res.*,
 1162 114, D08303, doi:10.1029/2008JD010621, 2009.
 1163 Park, R. J., Jacob, D. J., Chin, M., and Martin, R. V.: Sources of carbonaceous
 1164 aerosols over the United States and implications for natural visibility, *J.*
 1165 *Geophys. Res.*, 108, 4355, doi:10.1029/2002JD003190, 2003.
 1166 Park, R. J., Jacob, D. J., Field, B. D., Yantosca, R. M., and Chin, M.: Natural
 1167 and transboundary pollution influences on sulfate–nitrate–ammonium
 1168 aerosols in the United States: Implications for policy, *J. Geophys. Res.*,
 1169 109, D15204, doi:10.1029/2003JD004473, 2004.
 1170 Pitari, G., Aquila, V., Kravitz, B., Robock, A., Watanabe, S., Cionni, I., Luca, N.
 1171 D., Genova, G. D., Mancini, E., and Tilmes, S.: Stratospheric ozone
 1172 response to sulfate geoengineering: Results from the Geoengineering
 1173 Model Intercomparison Project (GeoMIP), *J. Geophys. Res.*, 119, 2629–
 1174 2653, doi: 10.1002/2013JD020566, 2014.
 1175 Popp, P., Marcy, T., Jensen, E., Kärcher, B., Fahey, D., Gao, R., Thompson, T.,
 1176 Rosenlof, K., Richard, E., and Herman, R.: The observation of nitric
 1177 acid-containing particles in the tropical lower stratosphere, *Atmos. Chem.*
 1178 *Phys.*, 6, 601–611, 2006.
 1179 Pye, H., Liao, H., Wu, S., Mickley, L. J., Jacob, D. J., Henze, D. K., and
 1180 Seinfeld, J.: Effect of changes in climate and emissions on future sulfate–
 1181 nitrate–ammonium aerosol levels in the United States, *J. Geophys. Res.*,
 1182 114, D01205, doi:10.1029/2008JD010701, 2009.
 1183 Qie, X., Wu, X., Yuan, T., Bian, J., and Lü, D.: Comprehensive Pattern of Deep
 1184 Convective Systems over the Tibetan Plateau–South Asian Monsoon
 1185 Region Based on TRMM Data, *J. Clim.*, 27, 6612–6626, 2014.
 1186 Ram, K., Sarin, M., and Hegde, P.: Atmospheric abundances of primary and
 1187 secondary carbonaceous species at two high-altitude sites in India:
 1188 Sources and temporal variability, *Atmos. Environ.*, 42, 6785–6796, 2008.
 1189 Ramanathan, V., Li, F., Ramana, M., Praveen, P., Kim, D., Corrigan, C.,
 1190 Nguyen, H., Stone, E. A., Schauer, J. J., and Carmichael, G.: Atmospheric
 1191 brown clouds: Hemispherical and regional variations in long-range
 1192 transport, absorption, and radiative forcing, *J. Geophys. Res.*, 112,
 1193 D22S21, doi:10.1029/2006JD008124, 2007.
 1194 Randel, W. J., and Park, M.: Deep convective influence on the Asian summer
 1195 monsoon anticyclone and associated tracer variability observed with

- 1196 Atmospheric Infrared Sounder (AIRS), *J. Geophys. Res.*, 111, D12314,
 1197 doi:10.1029/2005JD006490, 2006.
- 1198 Randel, W. J., Park, M., Emmons, L., Kinnison, D., Bernath, P., Walker, K. A.,
 1199 Boone, C., and Pumphrey, H.: Asian monsoon transport of pollution to the
 1200 stratosphere, *Science*, 328, 611–613, 2010.
- 1201 Rasch, P. J., Tilmes, S., Turco, R. P., Robock, A., Oman, L., Chen, C. C.,
 1202 Stenchikov, G. L., and Garcia, R. R.: An overview of geoengineering of
 1203 climate using stratospheric sulphate aerosols, *Philos. Trans. R. Soc.*
 1204 *A-Math. Phys. Eng. Sci.*, 366, 4007-4037, doi:10.1098/rsta.2008.0131,
 1205 2008.
- 1206 Rastogi, N., and Sarin, M.: Long-term characterization of ionic species in
 1207 aerosols from urban and high-altitude sites in western India: Role of
 1208 mineral dust and anthropogenic sources, *Atmos. Environ.*, 39, 5541–5554,
 1209 2005.
- 1210 Rastogi, N., and Sarin, M.: Quantitative chemical composition and
 1211 characteristics of aerosols over western India: one-year record of
 1212 temporal variability, *Atmos. Environ.*, 43, 3481–3488, 2009.
- 1213 Rengarajan, R., Sarin, M., and Sudheer, A.: Carbonaceous and inorganic
 1214 species in atmospheric aerosols during wintertime over urban and
 1215 high-altitude sites in North India, *J. Geophys. Res.*, 112, D21307,
 1216 doi:10.1029/2006JD008150, 2007.
- 1217 Russell, P. B., and McCormick, M. P.: SAGE II aerosol data validation and initial
 1218 data use: An introduction and overview, *J. Geophys. Res.*, 94, 8335–8338,
 1219 1989.
- 1220 Safai, P., Kewat, S., Praveen, P., Rao, P., Momin, G., Ali, K., and Devara, P.:
 1221 Seasonal variation of black carbon aerosols over a tropical urban city of
 1222 Pune, India, *Atmos. Environ.*, 41, 2699–2709, 2007.
- 1223 Salam, A., Bauer, H., Kassin, K., Mohammad Ullah, S., and Puxbaum, H.:
 1224 Aerosol chemical characteristics of a mega-city in Southeast Asia
 1225 (Dhaka–Bangladesh), *Atmos. Environ.*, 37, 2517–2528, 2003.
- 1226 Santee, M., Lambert, A., Read, W., Livesey, N., Cofield, R., Cuddy, D., Daffer,
 1227 W., Drouin, B., Froidevaux, L., and Fuller, R.: Validation of the Aura
 1228 Microwave Limb Sounder HNO₃ measurements, *J. Geophys. Res.*, 112,
 1229 D24S40, doi:10.1029/2007JD008721, 2007.
- 1230 Sauvage, B., Martin, R., Donkelaar, A. v., Liu, X., Chance, K., Jaeglé, L.,
 1231 Palmer, P., Wu, S., and Fu, T.-M.: Remote sensed and in situ constraints
 1232 on processes affecting tropical tropospheric ozone, *Atmos. Chem. Phys.*,
 1233 7, 815–838, 2007.
- 1234 Seinfeld, J. H., and Pandis, S. N.: Atmospheric chemistry and physics: from air
 1235 pollution to climate change, second ed. John Wiley: A Wiley-Interscience
 1236 Publication Press, 2006.
- 1237 Sharma, R. K., Bhattarai, B., Sapkota, B., Gewali, M., and Kjeldstad, B.: Black
 1238 carbon aerosols variation in Kathmandu valley, Nepal, *Atmos. Environ.*, 63,
 1239 282–288, doi:10.1016/j.atmosenv.2012.09.023, 2012.
- 1240 Shrestha, A. B., Wake, C. P., Dibb, J. E., Mayewski, P. A., Whitlow, S. I.,
 1241 Carmichael, G. R., and Ferm, M.: Seasonal variations in aerosol
 1242 concentrations and compositions in the Nepal Himalaya, *Atmos. Environ.*,
 1243 34, 3349–3363, 10.1016/s1352-2310(99)00366-0, 2000.
- 1244 Škerlak, B., Sprenger, M., and Wernli, H.: A global climatology of
 1245 stratosphere-troposphere exchange using the ERA-Interim data set from

1246 1979 to 2011, *Atmos. Chem. Phys.*, 14, 913–937, 2014.

1247 Stevenson, D. S., Dentener, F. J., Schultz, M. G., Ellingsen, K., Van Noije, T. P.

1248 C., Wild, O., Zeng, G., Amann, M., Atherton, C. S., and Bell, N.:

1249 Multimodel ensemble simulations of present-day and near-future

1250 tropospheric ozone, *J. Geophys. Res.*, 111, D08301,

1251 doi:10.1029/2005JD006338, 2006.

1252 Streets, D. G., Bond, T. C., Carmichael, G. R., Fernandes, S. D., Fu, Q., He, D.,

1253 Klimont, Z., Nelson, S. M., Tsai, N. Y., and Wang, M. Q.: An inventory of

1254 gaseous and primary aerosol emissions in Asia in the year 2000, *J.*

1255 *Geophys. Res.*, 108, GTE 30–31, 2003.

1256 Su, H., Jiang, J. H., Lu, X. H., Penner, J. E., Read, W. G., Massie, S.,

1257 Schoeberl, M. R., Colarco, P., Livesey, N. J., and Santee, M. L.: Observed

1258 Increase of TTL Temperature and Water Vapor in Polluted Clouds over

1259 Asia, *J. Clim.*, 24, 2728–2736, 10.1175/2010jcli3749.1, 2011.

1260 Sudheer, A., and Sarin, M.: Carbonaceous aerosols in MABL of Bay of Bengal:

1261 Influence of continental outflow, *Atmos. Environ.*, 42, 4089–4100, 2008.

1262 Talukdar, R. K., Burkholder, J. B., Roberts, J. M., Portmann, R. W., and

1263 Ravishankara, A.: Heterogeneous Interaction of N₂O₅ with HCl Doped

1264 H₂SO₄ under Stratospheric Conditions: ClNO₂ and Cl₂ Yields, *J. Phys.*

1265 *Chem. A.*, 116, 6003–6014, 2012.

1266 Tang, M., Telford, P., Pope, F., Rkiouak, L., Abraham, N., Archibald, A.,

1267 Braesicke, P., Pyle, J., McGregor, J., and Watson, I.: Heterogeneous

1268 reaction of N₂O₅ with airborne TiO₂ particles and its implication for

1269 stratospheric particle injection, *Atmos. Chem. Phys.*, 14, 6035–6048,

1270 2014.

1271 Tare, V., Tripathi, S., Chinnam, N., Srivastava, A., Dey, S., Manar, M.,

1272 Kanawade, V. P., Agarwal, A., Kishore, S., and Lal, R.: Measurements of

1273 atmospheric parameters during Indian Space Research Organization

1274 Geosphere Biosphere Program Land Campaign II at a typical location in

1275 the Ganga Basin: 2. chemical properties, *J. Geophys. Res.*, 111, D23210,

1276 doi:10.1029/2006JD007279, 2006.

1277 Thornton, J. A., Jaeglé, L., and McNeill, V. F.: Assessing known pathways for

1278 HO₂ loss in aqueous atmospheric aerosols: Regional and global impacts

1279 on tropospheric oxidants, *J. Geophys. Res.*, 113, D05303,

1280 doi:10.1029/2007JD009236, 2008.

1281 Tobo, Y., Zhang, D., Iwasaka, Y., and Shi, G.: On the mixture of aerosols and

1282 ice clouds over the Tibetan Plateau: Results of a balloon flight in the

1283 summer of 1999, *Geophys. Res. Lett.*, 34, L23801,

1284 doi:10.1029/2007GL031132, 2007.

1285 Tripathi, S., Dey, S., Tare, V., and Satheesh, S.: Aerosol black carbon radiative

1286 forcing at an industrial city in northern India, *Geophys. Res. Lett.*, 32,

1287 L08802, doi:10.1029/2005GL022515, 2005.

1288 van der Werf, G. R., Randerson, J. T., Giglio, L., Collatz, G. J., Mu, M.,

1289 Kasibhatla, P. S., Morton, D. C., DeFries, R. S., Jin, Y., and van Leeuwen,

1290 T. T.: Global fire emissions and the contribution of deforestation, savanna,

1291 forest, agricultural, and peat fires (1997–2009), *Atmos. Chem. Phys.*, 10,

1292 11707–11735, 2010.

1293 Vanhellefont, F., Tetard, C., Bourassa, A., Fromm, M., Dodion, J., Fussen, D.,

1294 Brogniez, C., Degenstein, D., Gilbert, K., and Turnbull, D.: Aerosol

1295 extinction profiles at 525 nm and 1020 nm derived from ACE imager data:

1296 comparisons with GOMOS, SAGE II, SAGE III, POAM III, and OSIRIS,
1297 Atmos. Chem. Phys., 8, 2027-2037, 2008.

1298 Venkataraman, C., Reddy, C. K., Josson, S., and Reddy, M. S.: Aerosol size
1299 and chemical characteristics at Mumbai, India, during the INDOEX-IFP
1300 (1999), Atmos. Environ., 36, 1979–1991, 2002.

1301 Verma, S., Boucher, O., Reddy, M., Upadhyaya, H., Van, P., Binkowski, F., and
1302 Sharma, O.: Tropospheric distribution of sulphate aerosols mass and
1303 number concentration during INDOEX-IFP and its transport over the
1304 Indian Ocean: a GCM study, Atmos. Chem. Phys., 12, 6185–6196, 2012.

1305 Vernier, J.-P., Pommereau, J.-P., Garnier, A., Pelon, J., Larsen, N., Nielsen, J.,
1306 Christensen, T., Cairo, F., Thomason, L., and Leblanc, T.: Tropical
1307 stratospheric aerosol layer from CALIPSO lidar observations, J. Geophys.
1308 Res., 114, D00H10, doi:10.1029/2009JD011946, 2009.

1309 Vernier, J. P., Thomason, L., and Kar, J.: CALIPSO detection of an Asian
1310 tropopause aerosol layer, Geophys. Res. Lett., 38, L07804,
1311 doi:10.1029/2010GL046614, 2011.

1312 Voigt, C., Schreiner, J., Kohlmann, A., Zink, P., Mauersberger, K., Larsen, N.,
1313 Deshler, T., Kröger, C., Rosen, J., and Adriani, A.: Nitric acid trihydrate
1314 (NAT) in polar stratospheric clouds, Science, 290, 1756-1758, 2000.

1315 Wang, P., McCormick, M., McMaster, L., Chu, W., Swissler, T., Osborn, M.,
1316 Russell, P., Oberbeck, V., Livingston, J., and Rosen, J.: SAGE II aerosol
1317 data validation based on retrieved aerosol model size distribution from
1318 SAGE II aerosol measurements, J. Geophys. Res., 94, 8381–8393,
1319 doi:10.1029/JD094iD06p08381, 1989.

1320 Wang, Y., Logan, J. A., and Jacob, D. J.: Global simulation of tropospheric O₃–
1321 NO_x–hydrocarbon chemistry: 2. Model evaluation and global ozone
1322 budget, J. Geophys. Res., 103, 10727–10755, 1998.

1323 Wang, Y., Zhang, Q., He, K., Zhang, Q., and Chai, L.:
1324 Sulfate-nitrate-ammonium aerosols over China: response to 2000–2015
1325 emission changes of sulfur dioxide, nitrogen oxides, and ammonia, Atmos.
1326 Chem. Phys., 13, 2635–2652, 2013.

1327 Waters, J. W., Froidevaux, L., Harwood, R. S., Jarnot, R. F., Pickett, H. M.,
1328 Read, W. G., Siegel, P. H., Cofield, R. E., Filipiak, M. J., and Flower, D.:
1329 The earth observing system microwave limb sounder (EOS MLS) on the
1330 Aura satellite, IEEE T. Geosci. Remote., 44, 1075-1092, 2006.

1331 Weigel, R., Borrmann, S., Kazil, J., Minikin, A., Stohl, A., Wilson, J., Reeves, J.,
1332 Kunkel, D., De Reus, M., and Frey, W.: In situ observations of new particle
1333 formation in the tropical upper troposphere: the role of clouds and the
1334 nucleation mechanism, Atmos. Chem. Phys. Discuss., 11, 2011.

1335 Wesely, M.: Parameterization of surface resistances to gaseous dry deposition
1336 in regional-scale numerical models, Atmos. Environ., 23, 1293-1304,
1337 1989.

1338 Wu, L. T., Su, H., and Jiang, J. H.: Regional simulations of deep convection
1339 and biomass burning over South America: 2. Biomass burning aerosol
1340 effects on clouds and precipitation, J. Geophys. Res., 116,
1341 doi:10.1029/2011jd016106, 2011.

1342 Wu, S., Mickley, L. J., Jacob, D. J., Logan, J. A., Yantosca, R. M., and Rind, D.:
1343 Why are there large differences between models in global budgets of
1344 tropospheric ozone? J. Geophys. Res., 112, D05302,
1345 doi:10.1029/2006JD007801, 2007.

1346 Wu, S., Mickley, L. J., Jacob, D. J., Rind, D., and Streets, D. G.: Effects of
1347 2000–2050 changes in climate and emissions on global tropospheric
1348 ozone and the policy–relevant background surface ozone in the United
1349 States, *J. Geophys. Res.*, 113, D18312, doi:10.1029/2007JD009639,
1350 2008.

1351 Xia, X., Zong, X., Cong, Z., Chen, H., Kang, S., and Wang, P.: Baseline
1352 continental aerosol over the central Tibetan plateau and a case study of
1353 aerosol transport from South Asia, *Atmos. Environ.*, 45, 7370–7378, 2011.

1354 Xiong, X., Houweling, S., Wei, J., Maddy, E., Sun, F., and Barnet, C.: Methane
1355 plume over south Asia during the monsoon season: satellite observation
1356 and model simulation, *Atmos. Chem. Phys.*, 9, 783–794, 2009.

1357 Yanai, M., Li, C., and Song, Z.: Seasonal heating of the Tibetan Plateau and its
1358 effects on the evolution of the Asian summer monsoon, *J. Meteorol. Soc.*
1359 *Jan.*, 70, 319–351, 1992.

1360 Yao, X., Chan, C. K., Fang, M., Cadle, S., Chan, T., Mulawa, P., He, K., and Ye,
1361 B.: The water-soluble ionic composition of PM_{2.5} in Shanghai and Beijing,
1362 China, *Atmos. Environ.*, 36, 4223–4234, 2002.

1363 Yin, Y., Chen, Q., Jin, L., Chen, B., Zhu, S., and Zhang, X.: The effects of deep
1364 convection on the concentration and size distribution of aerosol particles
1365 within the upper troposphere: A case study, *J. Geophys. Res.*, 117,
1366 D22202, doi:10.1029/2012JD017827, 2012.

1367 Zeng, G., Pyle, J., and Young, P.: Impact of climate change on tropospheric
1368 ozone and its global budgets, *Atmos. Chem. Phys.*, 8, 369–387, 2008.

1369 Zhang, G. J., and McFarlane, N. A.: Sensitivity of climate simulations to the
1370 parameterization of cumulus convection in the Canadian Climate Centre
1371 general circulation model, *Atmos.-Ocean*, 33, 407–446, 1995.

1372 Zhang, L., Liao, H., and Li, J.: Impacts of Asian summer monsoon on seasonal
1373 and interannual variations of aerosols over eastern China, *J. Geophys.*
1374 *Res.*, 115, D00K05, doi:10.1029/2009JD012299, 2010.

1375 Zhang, N., Cao, J., Ho, K., and He, Y.: Chemical characterization of aerosol
1376 collected at Mt. Yulong in wintertime on the southeastern Tibetan Plateau,
1377 *Atmos. Res.*, 107, 76, 2012.

1378 Zhang, Q., Streets, D. G., Carmichael, G. R., He, K., Huo, H., Kannari, A.,
1379 Klimont, Z., Park, I., Reddy, S., and Fu, J.: Asian emissions in 2006 for the
1380 NASA INTEX-B mission, *Atmos. Chem. Phys.*, 9, 5131–5153, 2009.

1381 Zhang, X., Cao, J., Li, L., Arimoto, R., Cheng, Y., Huebert, B., and Wang, D.:
1382 Characterization of atmospheric aerosol over Xian in the south margin of
1383 the Loess Plateau, China, *Atmos. Environ.*, 36, 4189–4199, 2002.

1384 Zhang, Y., Dore, A., Ma, L., Liu, X., Ma, W., Cape, J., and Zhang, F.:
1385 Agricultural ammonia emissions inventory and spatial distribution in the
1386 North China Plain, *Environ. Pollut.*, 158, 490–501, 2010.

1387 Zhao, X., Turco, R. P., Kao, C. Y. J., and Elliott, S.: Aerosol-induced chemical
1388 perturbations of stratospheric ozone: Three-dimensional simulations and
1389 analysis of mechanisms, *J. Geophys. Res.*, 102, 3617–3637,
1390 doi:10.1029/96jd03406, 1997.

1391 Zhu, J., Liao, H., and Li, J.: Increases in aerosol concentrations over
1392 eastern China due to the decadal-scale weakening of the East Asian
1393 summer monsoon, *Geophys. Res. Lett.*, 39, L09809,
1394 doi:10.1029/2012GL051428, 2012.

1395
1396

Table 1. Summary of Annual Emissions of Aerosols and Aerosol Precursors in Asia (60°E-155°E, 10°N-55°N)

Species	Global	Asia
NO_x (Tg N yr⁻¹)		
Aircraft	0.5	0.08
Anthropogenic	28.6	9.96
Biomass burning	4.7	0.27
Fertilizer	0.7	0.31
Lightning	5.9	0.87
Soil	5.9	0.96
Total	46.3	12.45
SO₂ (Tg S yr⁻¹)		
Aircraft	0.1	0.01
Anthropogenic	52.6	23.46
Biomass burning	1.2	0.07
Volcanoes	4.4	1.04
No_eruption	8.9	1.78
Ship	7.4	0.94
Total	74.6	27.30
NH₃ (Tg N yr⁻¹)		
Anthropogenic	34.9	17.83
Natural	14.2	2.01
Biomass burning	3.5	0.21
Biofuel	1.6	0.71
Total	54.2	20.76
OC (Tg C yr⁻¹)		
Anthropogenic	3.1	1.42
Biomass burning	18.7	1.10
Biofuel	6.3	3.28
Biogenic	9.7	1.22
Total	37.8	7.02
BC (Tg C yr⁻¹)		
Anthropogenic	3.0	1.43
Biomass burning	2.2	0.12
Biofuel	1.6	0.86
Total	6.8	2.41

1397
1398
1399
1400

Table 2. Simulated seasonal mean concentrations of aerosols and their contributions to PM_{2.5} (in percentages in parentheses) during summertime (June-August) of 2005 for the TP/SASM, TP, and SASM regions. The unit is $\mu\text{g m}^{-3}$ for concentrations at the surface, and $10^{-2} \mu\text{g m}^{-3}$ for concentrations at 200 hPa and 100 hPa.

	PM _{2.5}	SO ₄ ²⁻	NO ₃ ⁻	NH ₄ ⁺	OC	BC
TP/SASM						
Surface	4.73	1.70(35.9%)	0.94(19.8%)	0.85(18.1%)	0.94(19.8%)	0.30(6.4%)
200 hPa	16.19	3.27(20.2%)	7.57(46.8%)	2.67(16.5%)	2.22(13.7%)	0.44(2.7%)
100 hPa	12.14	2.60(21.4%)	6.90(56.8%)	1.43(11.8%)	1.05(8.6%)	0.16(1.3%)
TP						
Surface	5.44	2.12(39.0%)	1.05(19.3%)	1.08(19.9%)	0.88(16.1%)	0.31(5.7%)
200 hPa	19.80	4.16(21.0%)	9.43(47.6%)	3.25(16.4%)	2.49(12.6%)	0.47(2.4%)
100 hPa	10.58	2.60(24.6%)	5.51(52.0%)	1.35(12.7%)	0.99(9.4%)	0.14(1.3%)
SASM						
Surface	4.02	1.28(31.8%)	0.83(20.5%)	0.63(15.6%)	1.00(24.8%)	0.29(7.2%)
200 hPa	12.57	2.38(18.9%)	5.72(45.5%)	2.10(16.7%)	1.95(15.5%)	0.41(3.3%)
100 hPa	13.71	2.60(19.0%)	8.30(60.5%)	1.52(11.1%)	1.11(8.1%)	0.18(1.3%)

1401
1402

Table 3. List of gas-phase reactions and heterogeneous reactions involve HNO₃ in the GEOS-Chem model (Version 9-01-03)

	Reactants		Products
Chemical productions			
R1	NO ₂ + OH + M	→	HNO ₃ + M
R2	NO ₃ + CH ₂ O	→	HNO ₃ + prod.
R3	ALD ₂ + NO ₃	→	HNO ₃ + prod.
R4	RIO ₁ + NO	→	HNO ₃ + prod.
R5	IAO ₂ + NO	→	0.08HNO ₃ + prod.
R6	ISN ₁ + NO	→	0.05HNO ₃ + prod.
R7	VRO ₂ + NO	→	HNO ₃ + prod.
R8	MRO ₂ + NO	→	HNO ₃ + prod.
R9	INO ₂ +NO	→	0.85HNO ₃ + prod.
R10	ALK ₄ + NO ₃	→	HNO ₃ + prod.
R11	RCHO + NO ₃	→	HNO ₃ + prod.
R12	MEK + NO ₃	→	HNO ₃ + prod.
R13	INO ₂ + MO ₂	→	0.425HNO ₃ + prod.
R14	GLYX + NO ₃	→	HNO ₃ + prod.
R15	MGLY + NO ₃	→	HNO ₃ + prod.
R16	MACR + NO ₃	→	HNO ₃ + prod.
R17	C ₂ H ₆ + NO ₃	→	HNO ₃ + prod
R18	INO ₂ + MCO ₃	→	0.85HNO ₃ + prod.
R19	NO ₂ + (aerosol)	→	0.5HNO ₃ + prod.
R20	NO ₃ + (aerosol)	→	HNO ₃ + prod.
R21	N ₂ O ₅ + (aerosol)	→	2HNO ₃
R22	DMS + NO ₃	→	HNO ₃ + prod.
R23	BrNO ₃ + H ₂ O(l,s)	→	HNO ₃ + prod.
Chemical loss			
R24	HNO ₃ + OH	→	H ₂ O + NO ₃
R25	HNO ₃ + hv	→	OH + NO ₂

1403

1404 Table 4. Sensitivity simulations to examine the impacts of uncertainties in surface-layer aerosol concentrations on simulated NO_3^-
 1405 in the UTLS. “Conc” and “Ctr” denote, respectively, simulated seasonal mean concentrations of SO_4^{2-} , NO_3^- , NH_4^+ , OC, BC and
 1406 their contributions to $\text{PM}_{2.5}$ (in percentages) during summertime (June-August) of 2005. The mass concentrations are averaged
 1407 over the TP/SASM region, with unit of $\mu\text{g m}^{-3}$ at the surface layer and of $10^{-2} \mu\text{g m}^{-3}$ at 200 hPa and 100 hPa. Also shown are the
 1408 NMBs, as the simulated surface-layer concentrations are compared with measurements described in Section 4.2.

Species	Baseline Case			SO_2 (+20%)			NO_x (-50%)			NH_3 (-50%)			All Change		
	Conc.	Ctri.	NMB	Conc.	Ctri.	NMB	Conc.	Ctri.	NMB	Conc.	Ctri.	NMB	Conc.	Ctri.	NMB
Surface															
SO_4^{2-}	1.70	35.9%	-14.7%	1.92	38.1%	-4.4%	1.58	39.5%	-18.1%	1.70	38.1%	-14.7%	1.78	43.2%	-8.3%
NO_3^-	0.94	19.8%	+51.5%	0.94	18.7%	+53.5%	0.50	12.5%	-11.7%	0.73	16.4%	+24.1%	0.39	9.5%	-27.0%
NH_4^+	0.85	18.1%	+74.9%	0.94	18.6%	+93.8%	0.68	17.1%	+44.1%	0.78	17.6%	+64.6%	0.71	17.3%	+55.4%
OC	0.94	19.8%	-57.2%	0.94	18.6%	-57.2%	0.94	23.4%	-57.2%	0.94	21.0%	-57.2%	0.94	22.7%	-57.2%
BC	0.30	6.4%	-32.2%	0.30	6.0%	-32.2%	0.30	7.5%	-32.2%	0.30	6.8%	-32.2%	0.30	7.3%	-32.2%
200 hPa															
SO_4^{2-}	3.27	20.2%		3.67	22.9%		3.31	20.6%		3.29	29.1%		3.74	33.7%	
NO_3^-	7.57	46.8%		7.05	43.9%		7.41	46.0%		3.86	34.2%		3.19	28.7%	
NH_4^+	2.67	16.5%		2.67	16.6%		2.71	16.8%		1.49	13.2%		1.50	13.5%	
OC	2.22	13.7%		2.22	13.8%		2.22	13.8%		2.22	19.7%		2.22	20.0%	
BC	0.44	2.7%		0.44	2.7%		0.44	2.7%		0.44	3.9%		0.44	4.0%	
100 hPa															
SO_4^{2-}	2.60	21.4%		2.80	23.0%		2.66	21.9%		2.60	25.2%		2.87	27.2%	
NO_3^-	6.90	56.8%		6.72	55.3%		6.81	56.1%		5.68	55.0%		5.62	53.3%	
NH_4^+	1.43	11.8%		1.43	11.7%		1.45	12.0%		0.84	8.1%		0.84	8.0%	
OC	1.05	8.6%		1.05	8.6%		1.05	8.7%		1.05	10.2%		1.05	10.0%	
BC	0.16	1.3%		0.16	1.3%		0.16	1.3%		0.16	1.6%		0.16	1.5%	

1409 **Figure Captions**

1410

1411 **Figure. 1.** Regions examined in this study: the Tibetan Plateau region (TP, 70–
1412 105°E, 25–40°N), the SASM region (SASM, 70–105°E, 10–25°N), and the
1413 anticyclone region of (20–120°E, 10–40°N).

1414

1415 **Figure. 2.** Monthly variations in emissions of NO_x (Tg N month^{-1}), SO_2 (Tg S
1416 month^{-1}), NH_3 (Tg N month^{-1}), OC (Tg C month^{-1}), and BC (Tg C month^{-1})
1417 over Asia. Values shown are the total emissions (anthropogenic plus natural
1418 emissions listed in Table 1).

1419

1420 **Figure. 3.** Simulated global distributions of surface-layer HNO_3 (pptv) and O_3
1421 (ppbv) averaged over June-August, 2005.

1422

1423 **Figure. 4.** Comparisons of simulated HNO_3 concentrations (pptv) with
1424 observations (pptv) from MLS. (a) and (b) are simulated concentrations at 200
1425 hPa and 100 hPa, respectively. (c) is the latitude-altitude cross section of
1426 simulated HNO_3 concentrations averaged over 70–105°E. (d)-(f) are the same
1427 as (a)-(c), except that (d)-(f) are observations from MLS. The GEOS-Chem
1428 HNO_3 simulations are smoothed by the corresponding averaging kernels (AK).
1429 White areas indicate lack of data meeting the retrieval quality criteria. All the
1430 data are averaged over June-August of 2005.

1431

1432 **Figure. 5.** Comparisons of simulated O_3 concentrations (ppbv) with
1433 observations (ppbv) from MLS. (a) and (b) are simulated concentrations at 200
1434 hPa and 100 hPa, respectively. (c) is the latitude-altitude cross section of
1435 simulated O_3 concentrations averaged over 70–105°E. (d)-(f) are the same as
1436 (a)-(c), except that (d)-(f) are observations from MLS. The GEOS-Chem O_3
1437 simulations are smoothed by the corresponding averaging kernels. White
1438 areas indicate lack of data meeting the retrieval quality criteria. All the data are
1439 averaged over June-August of 2005.

1440

1441 **Figure. 6.** The simulated and observed vertical profiles of monthly mean O_3
1442 mixing ratios at (a) Kunming and (b) Lhasa in August. The model results are
1443 from the simulation of year 2005. The observations in Kunming were
1444 conducted during August 7–13 (11 profiles of O_3 collected) in 2009 and during
1445 August 12–31 in 2012 (daily observations). The observations in Lhasa were
1446 conducted during August 22–28 in 2010 (12 profiles of O_3 collected) and
1447 during August 4–26 in 2013 (daily observations).

1448

1449 **Figure. 7.** Simulated seasonal mean concentrations ($\mu\text{g m}^{-3}$) of sulfate, nitrate,
1450 ammonium, organic carbon, black carbon, and $\text{PM}_{2.5}$ at (a) the surface layer, (b)
1451 200 hPa, and (c) 100 hPa, during summer (June-August) of year 2005. Note
1452 that color bars are different for concentrations at the surface, 200 hPa, and 100
1453 hPa.

1454

1455 **Figure. 8.** (a) Locations with measured aerosol concentrations from previous
1456 studies. Also shown are surface winds during summertime. (b)–(f) show the
1457 comparisons of simulated seasonal mean concentrations of sulfate, nitrate,

1458 ammonium, OC, and BC with measured values, respectively. Also shown in
1459 (b)–(f) are the 1:1 line (dashed), linear fit (solid line and equation), correlation
1460 coefficient between simulated and measured concentrations (R), and
1461 normalized mean bias (NMB) (defined as $NMB = \frac{\sum_{i=1}^n (P_i - O_i)}{\sum_{i=1}^n O_i} \times 100\%$, where P_i
1462 and O_i are predicted and observed concentrations at station i for each aerosol
1463 species).

1464
1465 **Figure. 9.** (a) Monthly mean distribution of aerosol extinction coefficients (km^{-1})
1466 at 100 hPa for July of 2005. (b) Monthly mean vertical distributions of aerosol
1467 extinction coefficients (at 525 nm for SAGE II and 550 nm for GEOS-Chem)
1468 (km^{-1}) averaged over the Asian monsoon anticyclone region (20–120°E,
1469 10–40°N) for July of 2005. The horizontal dashed line represents the
1470 tropopause averaged over the Asian monsoon anticyclone region simulated by
1471 the GEOS-Chem model.

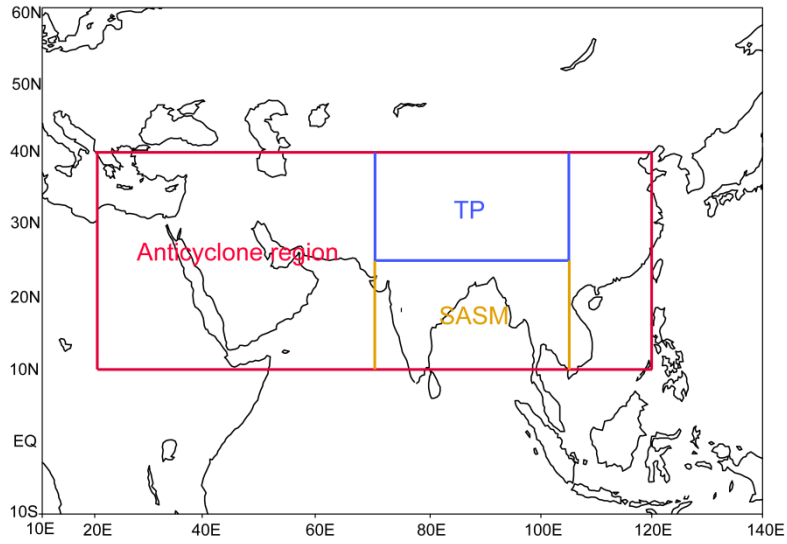
1472
1473 **Figure. 10.** Simulated contributions of nitrate to $\text{PM}_{2.5}$ ($C_{\text{NIT}} = [\text{NIT}] / [\text{PM}_{2.5}]$
1474 $\times 100\%$) averaged over summer (June–August) of year 2005 at (a)
1475 surface-layer, (b) 200 hPa, and (c) 100 hPa. (d) The latitude-altitude cross
1476 section of simulated C_{NIT} (%) averaged over 70–105°E.

1477
1478 **Figure. 11.** Latitude-altitude cross sections of simulated concentrations (color
1479 shades, $\mu\text{g m}^{-3}$) of SO_4^{2-} and NO_3^- averaged over 70–105°E in June–August
1480 of 2005, together with the wind vectors obtained from the European Centre for
1481 Medium-Range Weather Forecasts (ECMWF) ERA-Interim Reanalysis data.
1482 The black line is the tropopause simulated by the GEOS-Chem model.

1483
1484 **Figure. 12.** The net chemical production of HNO_3 by gas-phase reactions and
1485 heterogeneous reactions (black dotted line) and the production of nitrate from
1486 gas to aerosol conversion of HNO_3 (red dotted line) over the TP/SASM region
1487 during summertime of year 2005.

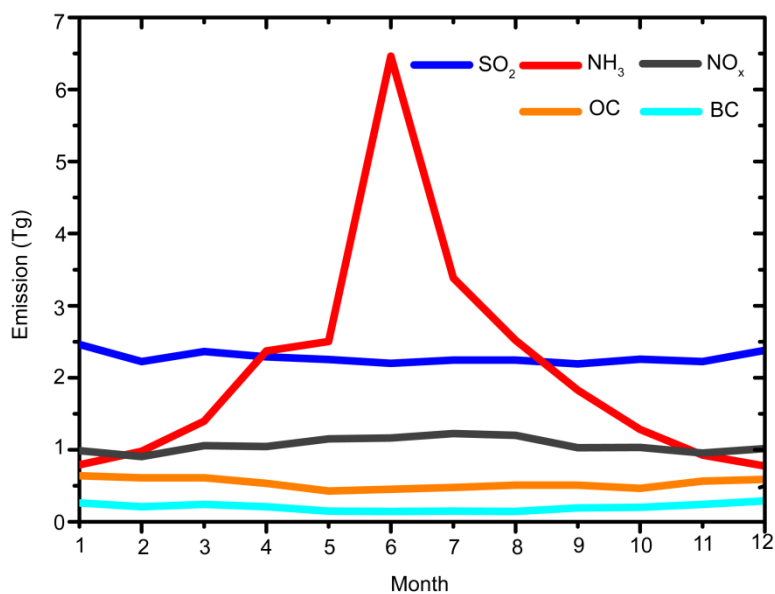
1488
1489 **Figure. 13.** (a)–(b) Distributions of RH (%) and temperature (K) at 100 hPa.
1490 (c)–(d) The latitude-altitude cross sections of RH (%) and temperature (K)
1491 averaged over 70–105°E. RH and temperature are from the GEOS5
1492 assimilated meteorological fields, and all the values are the averages over
1493 June–August of year 2005.

1494
1495 **Figure. 14.** Mass budget for nitrate aerosol within the selected box of (70–
1496 105°E, 10–40°N, 8–16 km). E/W transport indicates net mass flux through the
1497 east and west lateral boundaries, N/S transport indicates net mass flux through
1498 the north and south lateral boundaries, and upward transport is the net mass
1499 flux through the top and bottom sides of the box. The mass flux is positive if it
1500 increases nitrate mass within the box. Unit of fluxes is Tg season^{-1} . All the
1501 values are the averages over June–August of 2005.



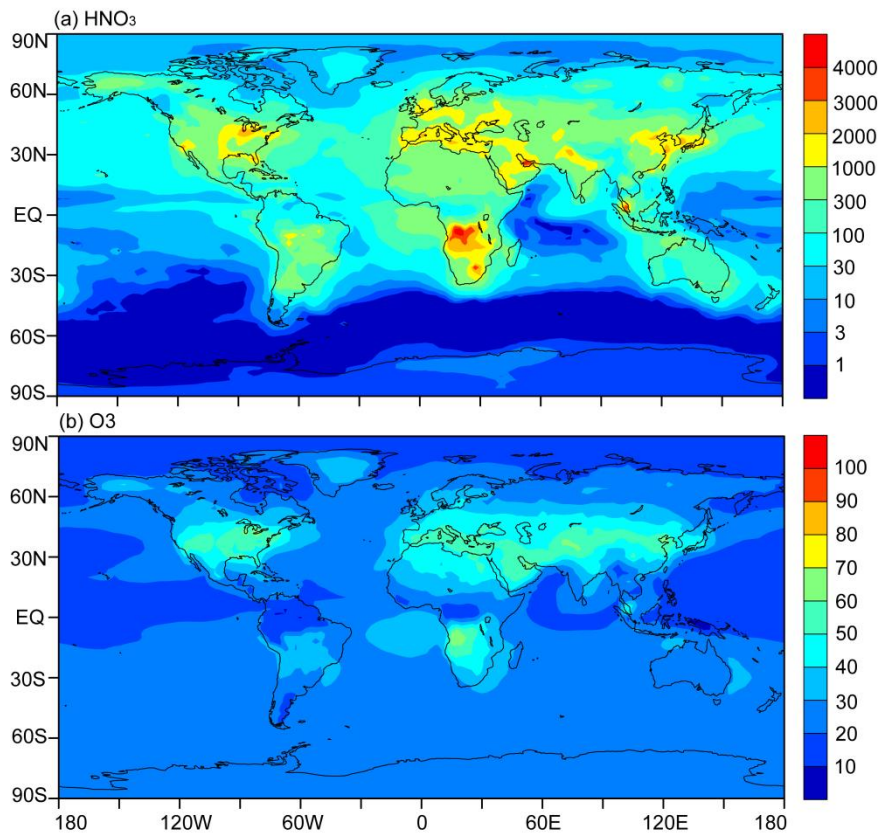
1502
 1503
 1504
 1505
 1506

Figure. 1. Regions examined in this study: the Tibetan Plateau region (TP, 70–105°E, 25–40°N), the SASM region (SASM, 70–105°E, 10–25°N), and the anticyclone region of (20–120°E, 10–40°N).



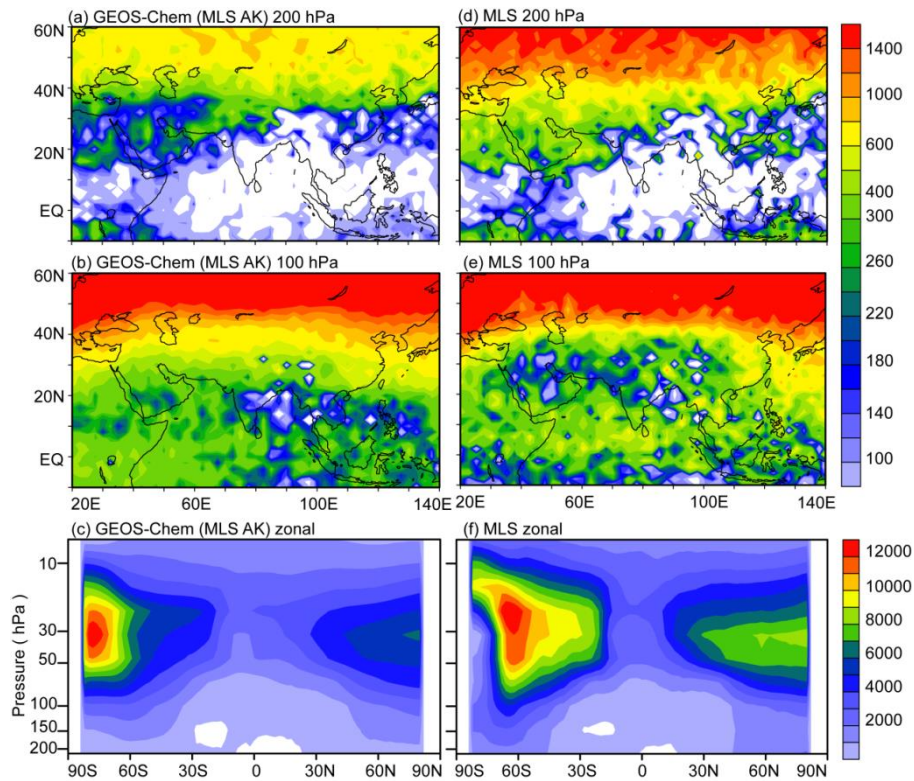
1507
 1508
 1509
 1510
 1511
 1512

Figure. 2. Monthly variations in emissions of NO_x (Tg N month⁻¹), SO₂ (Tg S month⁻¹), NH₃ (Tg N month⁻¹), OC (Tg C month⁻¹), and BC (Tg C month⁻¹) over Asia. Values shown are the total emissions (anthropogenic plus natural emissions listed in Table 1).



1513
 1514
 1515
 1516

Figure. 3. Simulated global distributions of surface-layer HNO_3 (pptv) and O_3 (ppbv) averaged over June-August, 2005.



1517

1518

1519

1520

1521

1522

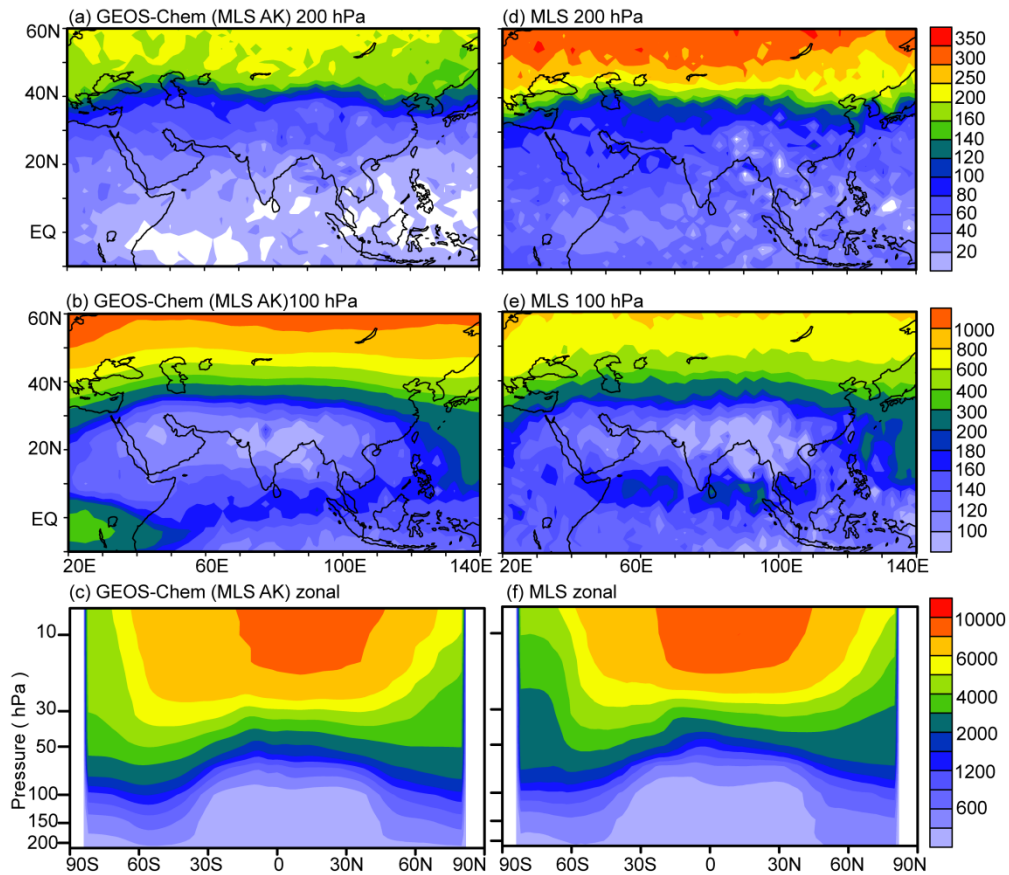
1523

1524

1525

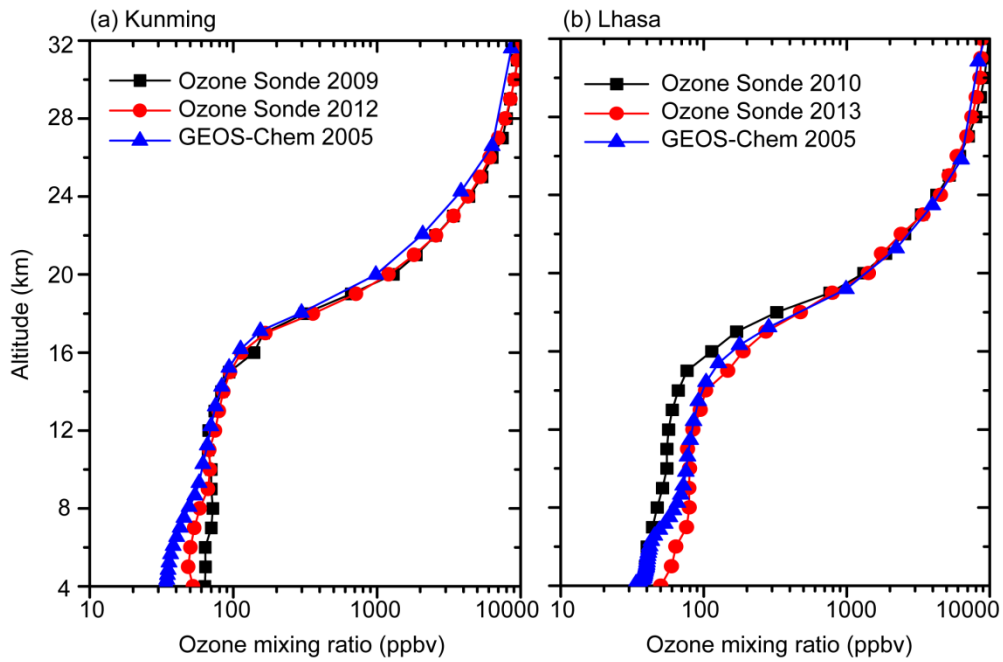
1526

Figure 4. Comparisons of simulated HNO_3 concentrations (pptv) with observations (pptv) from MLS. (a) and (b) are simulated concentrations at 200 hPa and 100 hPa, respectively. (c) is the latitude-altitude cross section of simulated HNO_3 concentrations averaged over 70–105°E. (d)-(f) are the same as (a)-(c), except that (d)-(f) are observations from MLS. The GEOS-Chem HNO_3 simulations are smoothed by the corresponding averaging kernels (AK). White areas indicate lack of data meeting the retrieval quality criteria. All the data are averaged over June-August of 2005.



1527
 1528
 1529
 1530
 1531
 1532
 1533
 1534
 1535
 1536

Figure. 5. Comparisons of simulated O_3 concentrations (ppbv) with observations (ppbv) from MLS. (a) and (b) are simulated concentrations at 200 hPa and 100 hPa, respectively. (c) is the latitude-altitude cross section of simulated O_3 concentrations averaged over 70–105°E. (d)-(f) are the same as (a)-(c), except that (d)-(f) are observations from MLS. The GEOS-Chem O_3 simulations are smoothed by the corresponding averaging kernels. White areas indicate lack of data meeting the retrieval quality criteria. All the data are averaged over June-August of 2005.



1537

1538

1539

1540

1541

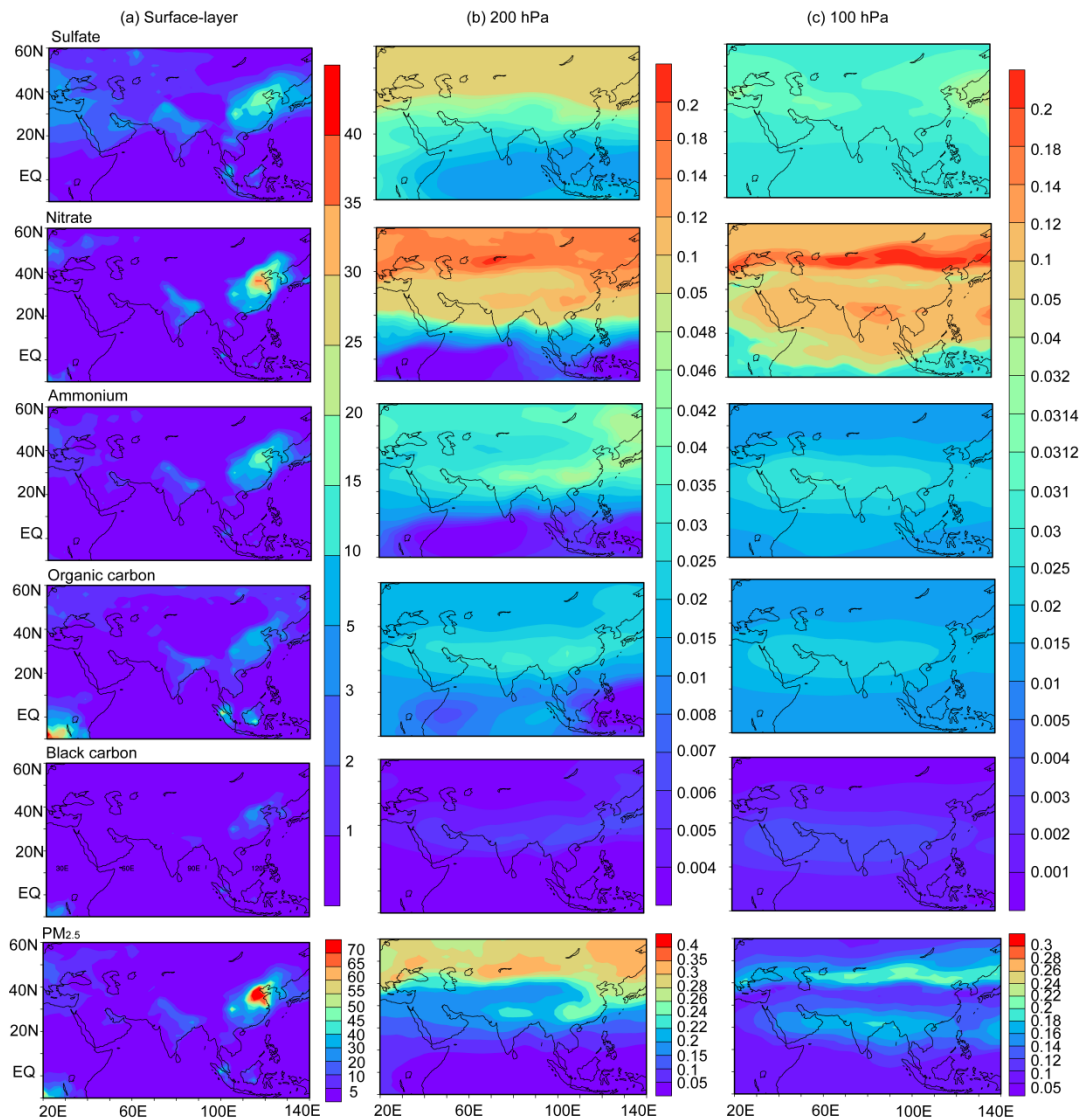
1542

1543

1544

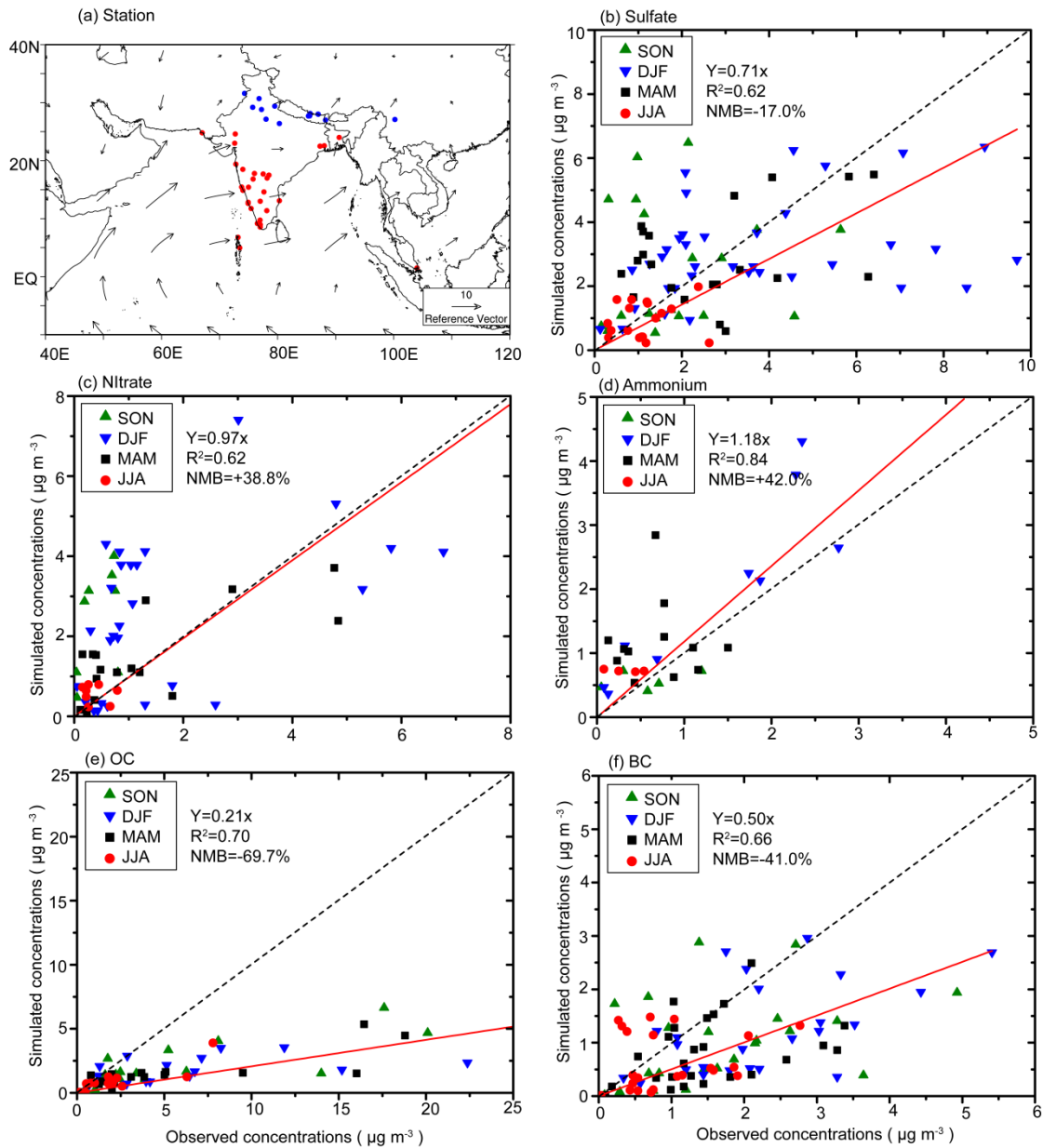
1545

Figure 6. The simulated and observed vertical profiles of monthly mean O₃ mixing ratios at (a) Kunming and (b) Lhasa in August. The model results are from the simulation of year 2005. The observations in Kunming were conducted during August 7–13 (11 profiles of O₃ collected) in 2009 and during August 12–31 in 2012 (daily observations). The observations in Lhasa were conducted during August 22–28 in 2010 (12 profiles of O₃ collected) and during August 4–26 in 2013 (daily observations).



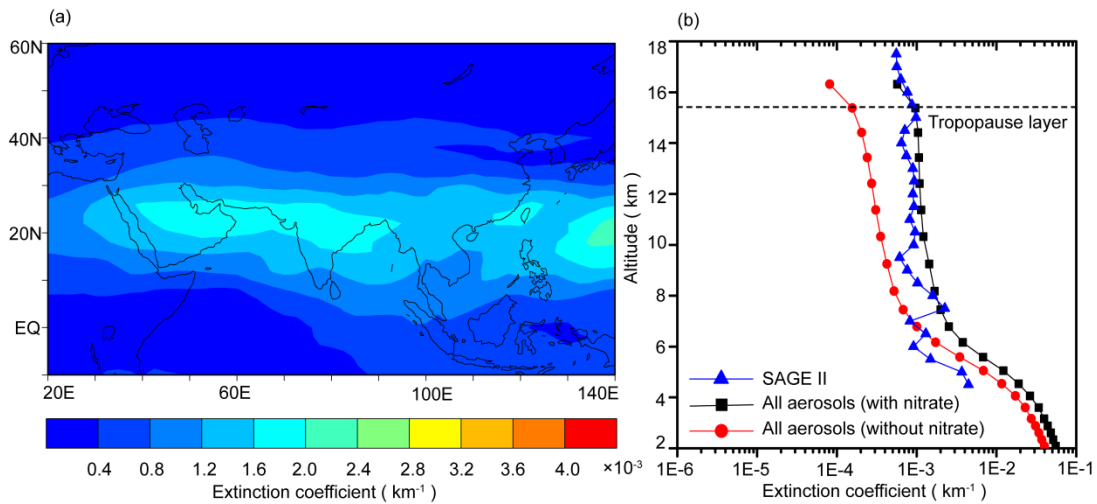
1546
1547

1548 **Figure. 7.** Simulated seasonal mean concentrations ($\mu\text{g m}^{-3}$) of sulfate, nitrate,
 1549 ammonium, organic carbon, black carbon, and $\text{PM}_{2.5}$ at (a) the surface layer, (b)
 1550 200 hPa, and (c) 100 hPa, during summer (June-August) of year 2005. Note
 1551 that color bars are different for concentrations at the surface, 200 hPa, and
 1552 hPa.



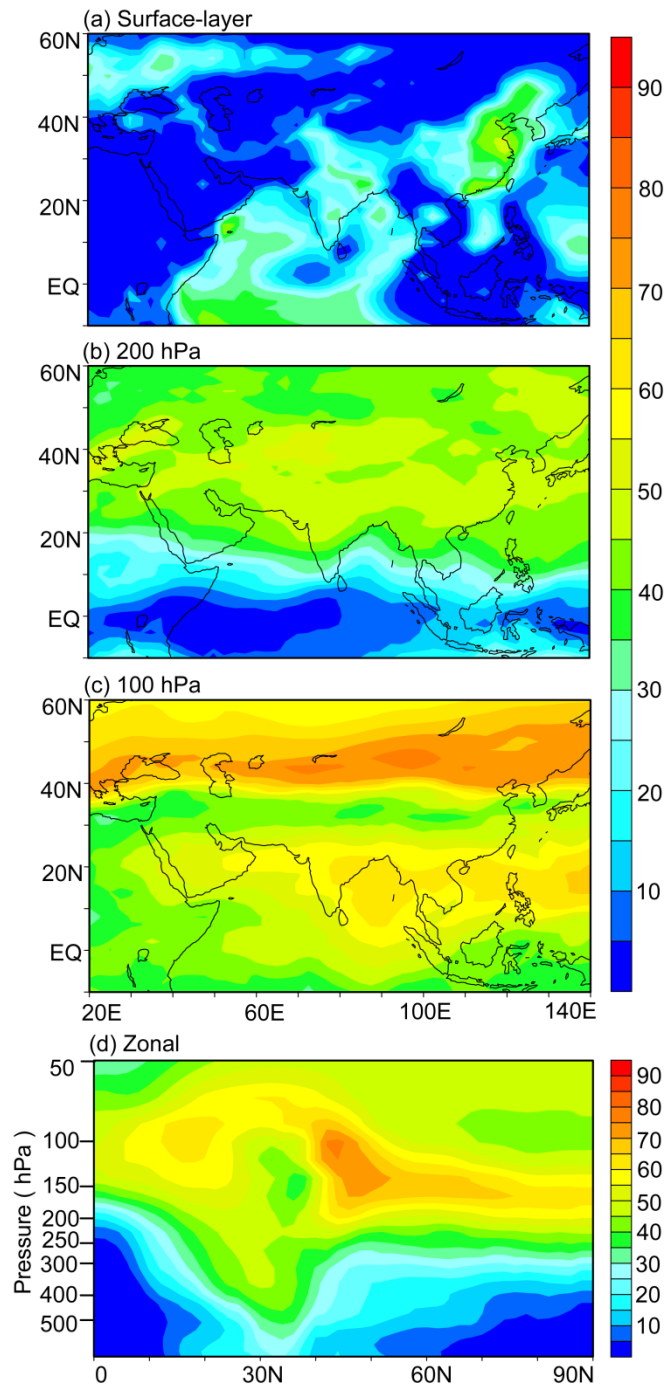
1553
1554

1555 **Figure 8.** (a) Locations with measured aerosol concentrations from previous
1556 studies over the TP (blue) and SASM (red) region. Also shown are surface
1557 winds during summertime. (b)–(f) show the comparisons of simulated seasonal
1558 mean concentrations of sulfate, nitrate, ammonium, OC, and BC with
1559 measured values, respectively. Also shown in (b)–(f) are the 1:1 line (dashed),
1560 linear fit (solid line and equation), correlation coefficient between simulated
1561 and measured concentrations (R), and normalized mean bias (NMB) (defined
1562 as $NMB = \frac{\sum_{i=1}^n (P_i - O_i)}{\sum_{i=1}^n O_i} \times 100\%$, where P_i and O_i are predicted and observed
1563 concentrations at station i for each aerosol species).



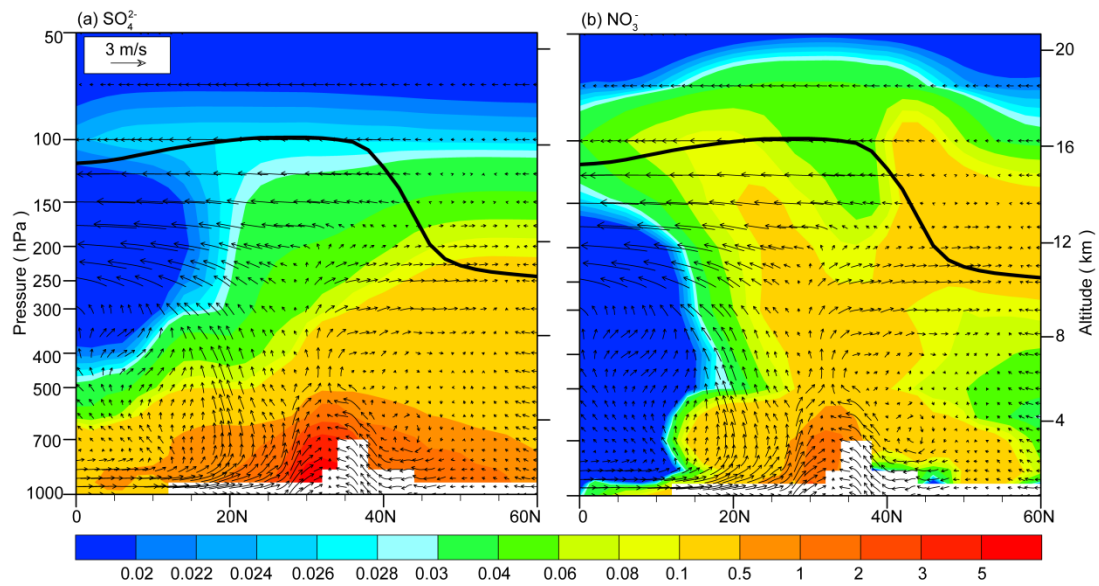
1564
1565

1566 **Figure. 9.** (a) Monthly mean distribution of aerosol extinction coefficients (km^{-1})
 1567 at 100 hPa for July of 2005. (b) Monthly mean vertical distributions of aerosol
 1568 extinction coefficients (at 525 nm for SAGE II and 550 nm for GEOS-Chem)
 1569 (km^{-1}) averaged over the Asian monsoon anticyclone region ($20\text{--}120^\circ\text{E}$,
 1570 $10\text{--}40^\circ\text{N}$) for July of 2005. The horizontal dashed line represents the
 1571 tropopause averaged over the Asian monsoon anticyclone region simulated by
 1572 the GEOS-Chem model.



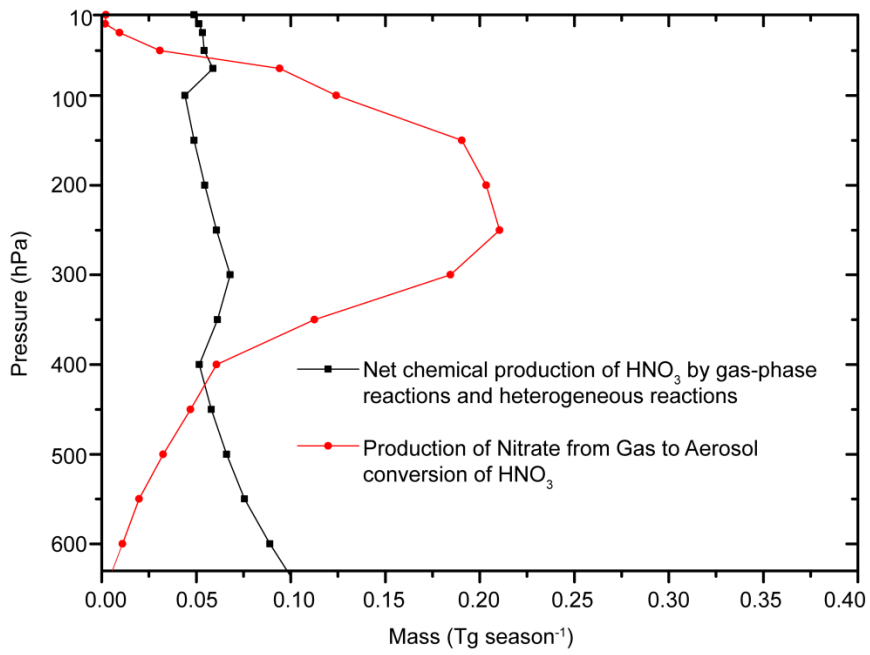
1573
 1574
 1575
 1576
 1577
 1578

Figure. 10. Simulated contributions of nitrate to $PM_{2.5}$ ($C_{NIT} = [NIT] / [PM_{2.5}] \times 100\%$) averaged over summer (June-August) of year 2005 at (a) surface-layer, (b) 200 hPa, and (c) 100 hPa. (d) The latitude-altitude cross section of simulated C_{NIT} (%) averaged over 70–105°E.



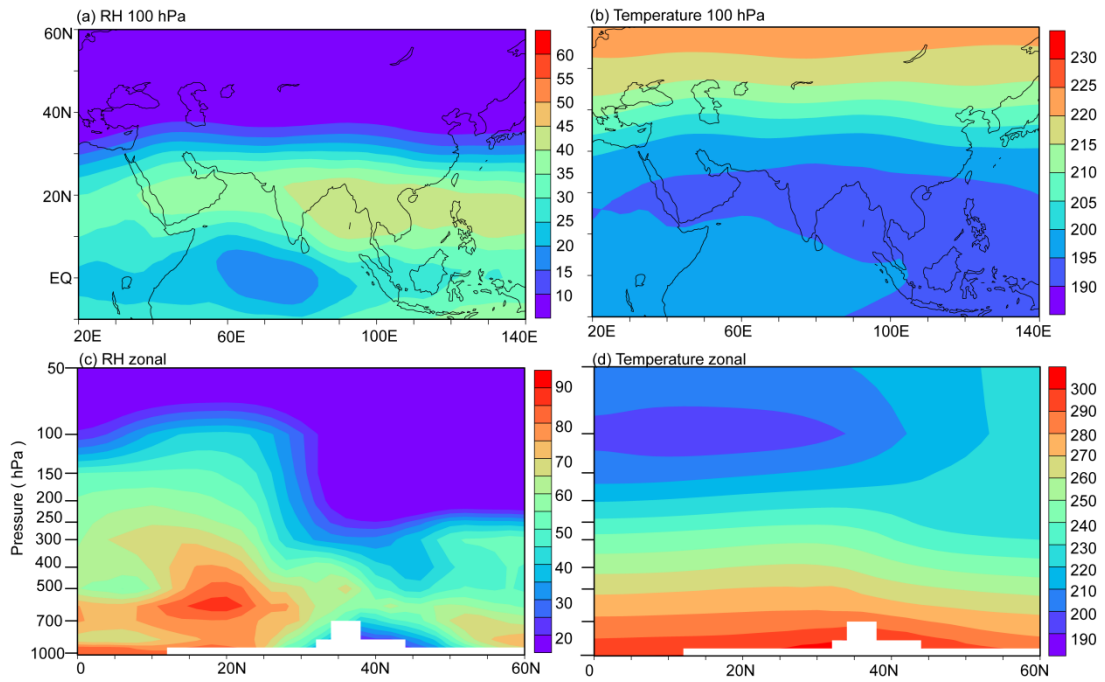
1579
 1580
 1581
 1582
 1583
 1584
 1585

Figure. 11. Latitude-altitude cross sections of simulated concentrations (color shades, $\mu\text{g m}^{-3}$) of SO_4^{2-} and NO_3^- averaged over $70\text{--}105^\circ\text{E}$ in June-August of 2005, together with the wind vectors obtained from the European Centre for Medium-Range Weather Forecasts (ECMWF) ERA-Interim Reanalysis data. The black line is the tropopause simulated by the GEOS-Chem model.



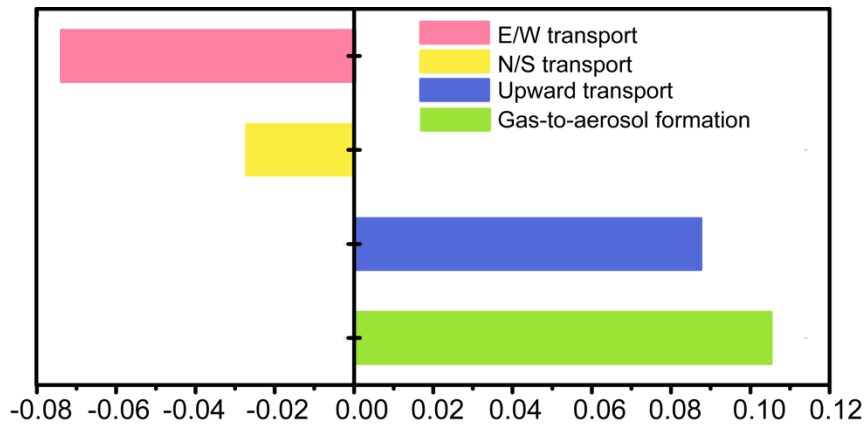
1586
 1587
 1588
 1589
 1590
 1591

Figure 12. The net chemical production of HNO₃ by gas-phase reactions and heterogeneous reactions (black dotted line) and the production of nitrate from gas to aerosol conversion of HNO₃ (red dotted line) over the TP/SASM region during summertime of year 2005.



1592
 1593
 1594
 1595
 1596
 1597
 1598

Figure. 13. (a)-(b) Distributions of RH (%) and temperature (K) at 100 hPa. (c)-(d) The latitude-altitude cross sections of RH (%) and temperature (K) averaged over 70–105°E. RH and temperature are from the GEOS5 assimilated meteorological fields, and all the values are the averages over June-August of year 2005.



1599
 1600
 1601
 1602
 1603
 1604
 1605
 1606
 1607

Figure. 14. Mass budget for nitrate aerosol within the selected box of (70–105°E, 10–40°N, 8–16 km). E/W transport indicates net mass flux through the east and west lateral boundaries, N/S transport indicates net mass flux through the north and south lateral boundaries, and upward transport is the net mass flux through the top and bottom sides of the box. The mass flux is positive if it increases nitrate mass within the box. Unit of fluxes is Tg season⁻¹. All the values are the averages over June-August of 2005.